The Topology of the Cosmic Web in Terms of Persistent Betti Numbers

Pratyush Pranav[1,2]*, Herbert Edelsbrunner[3], Rien van de Weygaert[1], Gert Vegter[4], Michael Kerber[6], Bernard J.T. Jones[1], and Mathijs Wintraecken[4,5]

[1] *Kapteyn Astronomical Institute, University of Groningen, P.O. Box 800, 9700AV Groningen, the Netherlands*
[2] *Technion - Israel Institute of Technology, Haifa, Israel 32000*
[3] *IST Austria (Institute of Science and Technology Austria), Klosterneuburg, Austria*
[4] *J.B. Institute for Mathematics and Computer Science, University of Groningen, the Netherlands*
[5] *INRIA Sophia Antipolis-Méditerranée, 2004 route des Lucioles - BP 93, 06902 Sophia Antipolis Cedex, France*
[6] *Institute of Geometry, Graz University of Technology, Kopernikusgasse 24, 8010 Graz, Austria*

15 August 2016

ABSTRACT
We introduce a multiscale topological description of the Megaparsec weblike cosmic matter distribution. Betti numbers and topological persistence offer a powerful means of describing the rich connectivity structure of the cosmic web and of its multiscale arrangement of matter and galaxies. Emanating from algebraic topology and Morse theory, Betti numbers and persistence diagrams represent an extension and deepening of the cosmologically familiar topological genus measure, and the related geometric Minkowski functionals. In addition to a description of the mathematical background, this study presents the computational procedure for computing Betti numbers and persistence diagrams for density field filtrations. The field may be computed starting from a discrete spatial distribution of galaxies or simulation particles. The main emphasis of this study concerns an extensive and systematic exploration of the imprint of different weblike morphologies and different levels of multiscale clustering in the corresponding computed Betti numbers and persistence diagrams. To this end, we use Voronoi clustering models as templates for a rich variety of weblike configurations, and the fractal-like Soneira-Peebles models exemplify a range of multiscale configurations. We have identified the clear imprint of cluster nodes, filaments, walls, and voids in persistence diagrams, along with that of the nested hierarchy of structures in multiscale point distributions. We conclude by outlining the potential of persistent topology for understanding the connectivity structure of the cosmic web, in large simulations of cosmic structure formation and in the challenging context of the observed galaxy distribution in large galaxy surveys.

Key words:
Cosmology: theory, cosmic web, large-scale structure of Universe.
Computational Geometry: Delaunay tessellations,
Delaunay tessellation field estimator;
Computational Topology: Betti numbers, persistent homology,
persistence diagrams.

1 INTRODUCTION

This study presents a substantial extension of the topological description of the galaxy and cosmic matter distribution. It involves a fundamental topological description of the cosmic mass distribution oriented towards quantifying the complex connectivity properties of the cosmic web (Bond et al. 1996; van de Weygaert & Bond 2008; Cautun et al. 2014). By means of Betti numbers, this study quantifies the various classes of topological features that result from the spatial organization of the various morphological components - nodes, filaments, walls, and voids - in the cosmic web. The complex multiscale topology that is manifestation of the hierarchical buildup of cosmic structures is quantified by the powerful language of persistent topology (Edelsbrunner & Harer 2010). The present work follows up on earlier preliminary work (Eldering 2005; van de Weygaert et al. 2010; van de Weygaert et al. 2011). The persistent analysis of the cosmic web is closely related to other studies applying aspects of Morse theory, in particular via the wa-

* pranav@astro.rug.nl

tershed transform, to describe the cosmic web (Platen et al. 2007; Aragón-Calvo et al. 2010; Sousbie 2011; Sousbie et al. 2011).

1.1 The Cosmic Web

The Megaparsec scale distribution of matter revealed by galaxy surveys features a complex network of interconnected filamentary galaxy associations. This network, which has become known as the *Cosmic Web* (Bond et al. 1996), contains structures from a few megaparsecs up to tens and even hundreds of megaparsecs of size. Galaxies and mass exist in a wispy web-like spatial arrangement consisting of dense compact clusters, elongated filaments, and sheet-like walls, amidst large near-empty voids, with similar patterns existing at earlier epochs, albeit over smaller scales. The multiscale nature of this mass distribution, marked by substructure over a wide range of scales and densities, has been clearly demonstrated by the maps of the nearby cosmos produced by large galaxy redshift surveys such as the 2dFGRS, the SDSS, and the 2MASS redshift surveys (Colless et al. 2003; Tegmark et al. 2004; Huchra et al. 2012), as well as by recently produced maps of the galaxy distribution at larger cosmic depths such as VIPERS (Guzzo & The Vipers Team 2013).

The Cosmic Web is one of the most striking examples of complex geometric patterns found in nature, and certainly the largest in terms of size. According to the *gravitational instability scenario* (Peebles 1980), cosmic structure grows from tiny primordial density and velocity perturbations. Once the gravitational clustering process has gone beyond the initial linear growth phase, we see the emergence of complex patterns and structures in the density field.

Highly illustrative of the intricacies of the structure formation process are the results of the state-of-the-art N-body computer simulations of cosmic structure formation (e.g. Springel 2005; Ishiyama et al. 2013; Vogelsberger et al. 2014). These simulations suggest that the observed cellular patterns are a prominent and natural aspect of cosmic structure formation. The simulations also reveal the distinct characteristics of the structure formation process: the anisotropic nature of the structures, as well as their hierarchical aggregation.

The existence of the the Cosmic Web is the manifestation of the generic anisotropic nature of gravitational collapse, resulting from the intrinsic anisotropy of gravitational forces induced by the inhomogeneities in the cosmic mass distribution. For a full understanding of the intricacies of the cosmic web, the relationship between these gravitational tidal forces, and the resulting deformation of the matter distribution is of key importance (Bond et al. 1996; van de Weygaert & Bond 2008).

Perhaps the most significant and characteristic property of the cosmic mass distribution is its hierarchical nature. As it develops out of a primordial density field of supposedly Gaussian fluctuations, structure builds up in a hierarchical fashion. The first objects to emerge are small. Their formation is followed by a gradual buildup of ever larger structures through the assembly of these smaller constituent features. In this way, the large massive galaxy or cluster halos have formed (see e.g. Kauffmann & White 1993; Lacey & Cole 1994). The filaments that dominate the observed cosmic web have been formed in a similar fashion, through the gradual merging of smaller tendrils. Even the population of the vast near-empty regions, the underndese voids that dominate and mark the topology of the universe on Megaparsec scales, have been recognized to follow the same hierarchical process (Sheth & van de Weygaert 2004; Aragon-Calvo & Szalay 2013).

It culminates in a scenario in which voids grow, merge and shrink, much as bubbles do in soapsuds. The hierarchical buildup of the cosmic web thus produces a multiscale pattern of structures and objects, comprising a wide range of spatial and mass scales.

It has remained a major challenge to characterize the structure, geometry and connectivity of the Cosmic Web. The complex spatial pattern – marked by a rich geometry with multiple morphologies and shapes, an intricate connectivity, a lack of structural symmetries, an intrinsic multiscale nature and a wide range of densities – eludes a sufficiently relevant and descriptive analysis by conventional instruments to quantify the arrangement of mass and galaxies. Many attempts to analyze the clustering of mass and galaxies at Megaparsec scales have been rather limited in their ability to describe and quantify, let alone identify, the features and components of the cosmic web. Measures like the two-point correlation function, which has been the mainstay of many cosmological studies over the past forty years (Peebles 1980), are not sensitive to the spatial complexity of patterns in the mass and galaxy distribution.

Only over the past few years have we seen the development and formulation of more sophisticated techniques that address the spatially complex Megaparsec scale patterns. Some of these involve the statistical evaluation of stochastic geometric concepts, such as the filament detection via a generalization of the classical Candy model or Bisous model (Stoica et al. 2005; Stoica et al. 2010; Tempel et al. 2012), others involve geometric inference formalisms (Chazal et al. 2009; Genovese et al. 2010; Chazal & Sun 2014) while we also see the proliferation of tessellation-based algorithms (González & Padilla 2010; van de Weygaert & Schaap 2009). A large class of formalisms is based on local geometric properties, expressed via the signature of the Hessian of the density field, of the tidal field, or of the shear of the velocity field (e.g. Aragón-Calvo et al. 2007b; Hahn et al. 2007; Bond et al. 2010; Forero-Romero et al. 2009; Libeskind et al. 2012; Cautun et al. 2013). While most of these existing methods have the downside of being defined on only one particular - and sometimes arbitrary - scale, the more elaborate MMF/Nexus framework explicitly takes into account the multiscale character of the cosmic mass distribution (Aragón-Calvo et al. 2007b; Cautun et al. 2013). Most closely connected to the dynamics of the cosmic web formation process are several recently proposed formalisms that look at the phase-space structure of the evolving mass distribution (Shandarin 2011; Neyrinck 2012; Abel et al. 2012). Noting that the emergence of nonlinear structures occurs at locations where different streams of the corresponding flow field cross each other, the phase-space sheet methods provide a dynamically based identification of their morphological nature. For example, walls correspond to three-stream regions while most filament regions involve five stream regions. A few other formalisms use the topological structure of the cosmic density field. The first examples are the Watershed Void Finder (Platen et al. 2007) and ZOBOV (Neyrinck 2008). They use the watershed transform to delineate the underdense void basins in the large scale universe (also see Sutter et al. 2014). Aragón-Calvo et al. (2010) expanded this to Spineweb, an elaborate framework for identifying all different morphological entities in the cosmic web. Spineweb shares its topological foundation with the Disperse formalism (Sousbie 2011; Sousbie et al. 2011), which has proven to be particularly succesful in outlining the filamentary spine of the cosmic web (for a further development also see Shivashankar et al. 2016).

1.2 Topology: Connectivity of the Cosmic Web

In this study we specifically address a central aspect of the Cosmic Web, the connectivity of its various structural components. The

way in which matter has distributed itself over the various structural components - such as walls, filaments, cluster nodes and voids - and the manner in which they connect up in the complex network of the cosmic web is a key aspect of the spatial structure of the cosmic mass distribution.

The branch of mathematics that addresses issues of shape and connectivity is topology. The cosmic mass distribution emerging in different cosmological scenarios will entail different spatial patterns, and we should expect to find its expression in subtle yet highly significant differences in topological characteristics. Existing topological descriptions have not yet addressed these in any substantial detail.

The first cosmological studies that focused on topological aspects of the cosmic mass distribution evaluated and analyzed the genus and Euler characteristic of the corresponding iso-density surfaces. Gott and collaborators (Gott et al. 1986; Hamilton et al. 1986) studied the genus as a function of density threshold. Later, more discriminative topological information became available with the introduction of Minkowski functionals (Mecke et al. 1994a; Schmalzing & Buchert 1997). However, nearly without exception these studies had a largely global character, often focussing on issues such as the statistical nature of the cosmic mass distribution. Following up on our earlier preliminary work (Eldering 2005; van de Weygaert et al. 2010; van de Weygaert et al. 2011), the present study represents a substantial extension of the topological arsenal used for description of the galaxy and cosmic matter distribution. Most significantly, it takes into account the intricate hierarchical and multiscale weblike spatial patterns into which mass has organized itself on Megaparsec scales.

Of particular interest and relevance for the present study is the way in which the different morphological features are spatially connected in the global weblike network. A few characteristic examples illustrate this. A configuration of interconnected walls that enclose low-density void cavities represents an entirely different topological pattern than a percolating network of mutually connected elongated filaments. The latter would facilitate the connection of all underdense regions into a percolating valley with a sponge-like topology. The former is more reminiscent of a cheese-like configuration of cavities enclosed by high-density filaments and walls.

For a more detailed assessment, we would therefore want to understand the role of individual walls, filaments and other mass concentrations in outlining the topological structure. A key aspect of this quest is the topological imprint of the multiscale nature of the weblike mass distribution. It concerns the way in which the smaller scale features of the structural hierarchy are embedded in or emanate from the prominent large scale features of the cosmic web, and in particular how this is reflected in its topological character. It involves questions such as how topology may help us to probe the nature and scale of the dominant filamentary network that defines the spine of the cosmic web and to quantify the extent to which it branches off in a multiscale tapestry of ever smaller tendrils (see e.g. Aragón-Calvo et al. 2007a; Cautun et al. 2014). Equally interesting is the prospect of having a profound and well-defined quantitative characterization of the multiscale void population, the product of the hierarchically evolving soapsuds of voids outlining the segmentation of the Megaparsec scale Universe.

1.3 Homology

As indicated above, there is ample motivation to extend topological analysis beyond global characterizations such as genus, and to orient the description towards the identification of the underlying connections and details of the topological structure. Following this motivation and rationale, the prime purpose of our study is the introduction of a fundamental topological formalism that addresses the issues outlined above. These well-known mathematical concepts will equip cosmologists with new and potent methods for a more profound analysis of spatial patterns encountered in the Megaparsec scale universe.

The formalism that we introduce here finds its roots in algebraic topology and in Morse theory (Milnor 1963; Edelsbrunner & Harer 2010). Algebraic topology is the branch of mathematics that uses tools from abstract algebra to study topological spaces. It accomplishes this by establishing the correspondence between topological spaces and objects on the one hand and algebraic *groups* on the other hand. This allows one to formulate statements about topological spaces into the language of group theory, offering substantial flexibility and a deeper understanding of spatial structure and connectivities. It provides us with a global characterization of structural topology in terms of *Betti numbers* (e.g. Betti 1871; Edelsbrunner & Harer 2010). It also forms the foundation for the subsequent investigation of the hierarchical aspects of the topological structure of the cosmic mass distribution. This leads us to the introduction of the formalism of *persistent homology* (Edelsbrunner et al. 2002; Zomorodian et al. 2005; Carlsson et al. 2005; Carlsson & Zomorodian 2009; Carlsson 2009; Edelsbrunner & Harer 2010).

The specific formalism from algebraic topology that we use to describe the topological structure of the space defined by the cosmic density distribution is known as *homology*. This is the mathematical formalism for the quantitative characterization of the connectivity of space by assessing the presence and identity of the holes, usually via the description of the boundaries of these holes (Munkres 1984). The original motivation for homology was the observation that two topological spaces may be distinguished by examining their holes. In homology, *holes* are a key concept. In general, for a manifold or a more general topological space embedded in d-dimensional Euclidean space, there are d different types of holes, of dimension 0 to $d-1$. A three-dimensional topological space may contain 3 different species of holes. Restricting to 3D space, these holes have an intuitive interpretation. A 0-dimensional hole is the *gap* between two separate objects or *components*. A 1-dimensional hole is a *tunnel* through which one may pass in either direction without encountering a boundary. A *cavity* or *void* is a 2-dimensional hole, fully enclosed within a 2-dimensional surface or *shell*.

A central consideration of homology is that the identification of holes may be conveniently and unequivocally achieved on the basis of the boundary that surrounds them. For instance, while a disk is a 2-dimensional surface, a circle is only the 1-dimensional boundary of a disk. The circle has a 1-dimensional hole formed by puncturing the disk; the disk has no such hole. Along the same vein, a sphere is not a circle because it encloses a two-dimensional hole while the circle encloses a one-dimensional hole. These considerations lead homology to describe and classify topological spaces according to their boundary. Homology characterizes the boundaries in terms of *cycles*. Loosely speaking, cycles are closed loops, or submanifolds, that can be drawn on a given topological space. They are classified by dimension: a 0-cyle is a connected object or point, a 1-cycle is a closed *loop*, and a 2-cycle is a *shell*. Cutting along a 0-cycle corresponds to puncturing the topological space, while cutting along a 1-cycle yields either a disconnected piece or a simpler shape.

The concept of cycles can be translated into the language of group theory. Two p-cycles are called *homologous* when together

they bound a $(p+1)$-dimensional part of the space. This is the technical sense in which the two cycles are considered to be the same. Extrapolating these observations, we find that cycles can be arranged into homology groups. The collection of all p-dimensional cycles in the topological space forms the p-th *homology group H_p*. In this paper, all homology groups will be vector spaces, and in this case the *rank* of H_p is its dimension, namely the number of *independent p*-dimensional cycles in a topological space. This is the formal definition for the *Betti numbers β_p* (Betti 1871; Edelsbrunner & Harer 2010), where $p = 0, 1, \ldots, d$. Like the Euler characteristic, the Betti numbers are topological invariants of a space, meaning that they do not change under systematic transformations like rotation, translation and deformation. The first three Betti numbers have intuitive meanings: β_0 counts the number of isolated components, β_1 counts the numbers of loops enclosing independent tunnels and β_2 counts the number of shells enclosing separate voids. Betti numbers contain more topological information than the Euler characteristic χ, as may be directly appreciated and inferred from the fundamental *Euler-Poincaré Formula* (Edelsbrunner & Harer 2010; Adler & Taylor 2010). This states that χ is the alternating sum of all d Betti numbers. In other words, any one given value of the Euler characteristic lies on a $(d-1)$-dimensional hyperplane of corresponding possible combinations of Betti numbers $(\beta_0, \beta_1, \ldots, \beta_{d-1})$. This has important repercussions for the topological description of the cosmic mass distribution: even when having the same Euler characteristic or genus, a space - such as defined by the level set of a density field - may differ topologically in terms of their Betti numbers.

1.4 Persistence

The details of the spatial connections between the various topological spaces, holes or boundaries underlying the global homology properties, leads to the concept of *persistence* (Edelsbrunner et al. 2002; Edelsbrunner & Harer 2010). Persistence formalizes topology as a hierarchical concept, and represents a substantially richer characterization of the topological structure of the cosmic mass distribution than that specified by conventional descriptions in terms of genus and even Betti numbers. It is based on the realization that there is a wealth of topological information to be gained from a systematic analysis of the singularity structure of a field.

A central role is played by Morse theory, the branch of mathematics that studies the singularity structure of a field, ie. the position of minima, maxima and saddle points and their mutual connections. Of fundamental importance in this is the mathematical tenet that there is a close relationship between the topology of the space [1] and the critical points of any smooth function on the topological space (Milnor 1963; Edelsbrunner & Harer 2010). Following this observation, Morse theory describes the topology of the space by studying the critical points of a corresponding *Morse function*, i.e a smooth scalar function defined on the topological space. Submanifolds defined as the regions where the Morse function is in excess of a particular functional threshold value (superlevel sets) are topologically equivalent or, more precisely, *diffeomorphic* when the interval between the two defining threshold values does not contain any critical point. The important implication of this is that all changes in topology of a space occur only at critical points.

Armed with this knowledge, one may identify the connection

of individual topological features to the overall cosmic mass distribution. To this end, we use the fact that the critical points of the density field, or other fields related to the mass distribution, are not only responsible for the *formation* of a feature, but also for their *destruction*. By varying the density threshold, a topological feature — e.g. a component, tunnel, or a cavity — may emerge, disappear, or connect up with other features, as the topology of the space changes while passing through a critical value [2]. In the language of persistence, this marks the *birth* or *death* of a feature. In the case of a merger of features, the *elder rule* specifies that the elder feature survives. It is the nature of the critical point, i.e. its *index*, that decides what kind of feature is formed or destroyed.

Generically, the addalition of an index-p critical point may result in either the birth of a p-dimensional hole or the death of a $(p-1)$-dimensional one (Edelsbrunner et al. 2002; Zomorodian & Carlsson 2005; Edelsbrunner & Harer 2010). In the situation in which the submanifolds are identified with the superlevel sets of the density field, i.e., the regions where the density is higher than a particular density threshold, a saddle point may merge two distinct islands in the density field. Alternatively, it may connect different ends of the boundary of a singular connected object. While the first will lead to the loss of one island, the latter will lead to the birth of a new loop. Another example is that of a cavity that gets filled up entirely and disappear as we pass through a (local) minimum. By establishing how the different features merge and form ever larger structural complexes as the density threshold is decreased, we establish a tree of hierarchically nested topological features. In a sense, this is not unlike the cosmologically more familiar merging trees that are defined by the dynamical evolution of dark matter halos or voids (Parkinson et al. 2008; Behroozi et al. 2013).

The full hierarchical embedding of topological features may subsequently be recorded and summarized in a *persistence diagram* (Edelsbrunner et al. 2002; Edelsbrunner & Harer 2010) or *persistence barcode* (Zomorodian & Carlsson 2005; Carlsson et al. 2005; Carlsson 2009). For each ambient dimension $p = 0, 1, \ldots, d-1$ of a topological space, a persistence diagram records the *birth* and *death* of each topological feature or p-dimensional hole. For each hole i it plots the function value b_i at which the feature is created and the value d_i at which it disappears. 0-dimensional diagrams record the merger events of two separate islands, 1-dimensional ones the formation and destruction of loops, while 2-dimensional diagrams record the birth and death of cavities or voids. The resulting persistence diagrams consists of the collection of points (b_i, d_i), each point associated with a unique topological change in the space. The life-span of a topological feature, i.e. the absolute difference between its death and birth values, is the *persistence* value π, of the feature.

Persistence diagrams contain strictly more information than the Betti numbers: the p-th Betti number of the superlevel set for threshold value ν is the number of points in the region of the persistence diagram delineating features that are created at higher function values and destroyed at lower function values. The important implication of this is that persistence, Betti number and Euler characteristic contain strictly decreasing amount of topological information about a space. Based on his observation, and taking into account that persistent homology is hierarchical in nature, it is evident that persistent homology entails a considerably more complete characterization of the geometry and topology of the cosmic mass distribution.

---

[1] The *space* here refers to a *topological space*, and not the space in the sense of *space-time*, that cosmologists are more familiar with.

[2] a *critical value* is the value of a function at the *critical point*

Besides yielding a powerful statistical characterization of the topological structure of a space, the potential applications of persistence are numerous. One particularly interesting example in practical astronomical circumstances is that of filtering out insignificant noise features. In general, low-persistence features are more likely to be topological noise, while those with a high persistence values would correspond to real signals. In fact, persistence based filtering has the potential of substantially more profound applications. Indeed, in the context of complex spatial structures, such as the cosmic web, it has proven that it enables a better defined identification of individual features than conventional kernel filtering (Gyulassy et al. 2012; Sousbie 2011; Sousbie et al. 2011; Chazal & Sun 2014; Shivashankar et al. 2016). In particular noteworthy is the Disperse algorithm developed by Sousbie and collaborators for the identification of filaments and other structures in the large scale Universe (Sousbie 2011; Sousbie et al. 2011). The concept of persistence based filtering has a rich potential for tuning it to specific problems and circumstances, as was demonstrated in the recent Felix algorithm for filament detection in different weblike environments, such as voids or around rich cluster nodes (Shivashankar et al. 2016).

1.5 Persistent Topology of the Cosmic Web

The obvious aim of our work is the application of homology and persistence measures for analyzing the observed spatial distribution of galaxies and matter on Megaparsec scales. The ultimate purpose is to develop and further our understanding and appreciation for the spatial connectivity aspects of the cosmic web. The expectation is that it will help us to uncover aspects of spatial clustering that have hitherto remained unexplored in cosmological research. To be able to interpret the quantitative results obtained by such an analysis, it is necessary to have a guidance for the significance of the obtained measurements.

The complex reality of the observed galaxy distribution or that of a full-fledged computer simulation is the result of the intricate interplay between a range of physical processes. It manifests itself in a complex superposition, over a wide range of scales, of a rich variety of morphological features. In this respect, we encounter the complication that as yet there is no real insight or understanding for the expected behaviour of homology and persistence in complex spatial patterns such as the cosmic web. Almost without any exception there are no realistic physical situations and configurations for which exact analytical results for the corresponding measures are available. Even for the cosmologically canonical reference configuration of Gaussian random fields, there are no exact results for Betti numbers and persistence diagrams (but see Feldbrugge et al. 2015).

Instead of directly analyzing full-fledged realistic cosmological situations, such as the outcome of N-body computer simulations of structure formation in the concordance ΛCDM cosmology (see e.g. Springel 2005; Ishiyama et al. 2013; Vogelsberger et al. 2014; Schaye et al. 2015), we therefore first need to design a baseline reference. For the understanding and interpretation of the obtained homology and persistence measures, and to have the ability to obtain insight into their significance, we will need to equip ourselves with reference templates of these measures. The principal aim of this paper is exactly this. The reference templates will be the outcome of the topological analysis for a well-defined set of heuristic spatial models that each single out one particular characteristic aspect of the Cosmic Web. Each of the templates should provide insight and information on the impact of specific and well-defined spatial configurations on the values of Betti numbers and behavior

of persistence diagrams. Armed with these templates, we will have the ability to interpret and understand the topological measures obtained for the considerably more complex reality of the real, or simulated, universe. The full homology and persistence analysis of the mass, halo, and galaxy distribution in cosmological simulations will be the subject of a series of upcoming works (for the first results, see e.g. Nevenzeel (2013)). An additional study would involve the analysis of a set of mock galaxy catalogues that incorporate galaxy biasing effects as well as survey selection effects of known galaxy redshift surveys.

We use Voronoi clustering models (van de Weygaert & Icke 1989; van de Weygaert 1994, 2002; Aragón-Calvo et al. 2010) for investigating the manifestation of weblike and/or void-dominated configurations in topological measures. For the impact of the multiscale aspects of the clustering of galaxies, we use the fractal-like point distributions of the Soneira-Peebles model (Soneira & Peebles 1978).

The Voronoi clustering models are a versatile and useful class of models for the anisotropic and void-dominated nature of the Megaparsec mass distribution (van de Weygaert 1994, 2002). They use Voronoi tessellations as a spatial template for the weblike distribution of mass and galaxies, by a stochastic process of distributing particles in the various elements of the tessellations, ie. in the nodes, edges, planar faces and cell interiors of the tessellations (van de Weygaert & Icke 1989; van de Weygaert 1991, 2002; Aragón-Calvo et al. 2010). The Voronoi clustering models are flexible and can be tuned to represent a network of interconnected filaments, or a cellular distribution dominated by walls, or a pattern of massive compact cluster nodes or any combination of these. In turn, this enables us to calibrate and assess quantitatively the way in which such configurations manifest themselves in the topological measures obtained (see e.g. Shivashankar et al. 2016).

The Soneira-Peebles model (Soneira & Peebles 1978) produces fractal-like point distributions that allow a systematic exploration of the influence of the multiscale clustering of galaxies and mass. It involves the nested embedding of a sequence of nodes in a hierarchical treelike structure. The spatial clustering of the resulting fractal point distribution can be tuned quantitatively by means of a few defining parameters (also see Schaap 2007; van de Weygaert & Schaap 2009). We should note that while the Soneira-Peebles model represents a versatile and useful heuristic model for exploring the effects of the multiscale spatial clustering, the observed galaxy distribution is certainly not fully fractal (see e.g. Martinez & Jones 1990).

1.6 The Computational Formalism

The second major aim of this paper concerns the presentation of the computational formalism for calculating homology measures and persistence diagrams. The mathematical primer on topology in Section 4 therefore also includes extensive discussion of the computational machinery that we use to compute persistence diagrams and Betti numbers. The cosmological context defines a range of practical issues.

The principal issue is the fact that the density field is sampled by a discrete set of points, either particles in a computer simulation or galaxies in observational circumstances. Most of the topological studies in cosmology depend on some sort of user-specific smoothing and related threshold to specify surfaces of which the topology may be determined. In cosmological studies, this usually concerns isodensity surfaces and/or density superlevel and sublevel sets defined on a Gaussian filter scale. Given that we do not have available
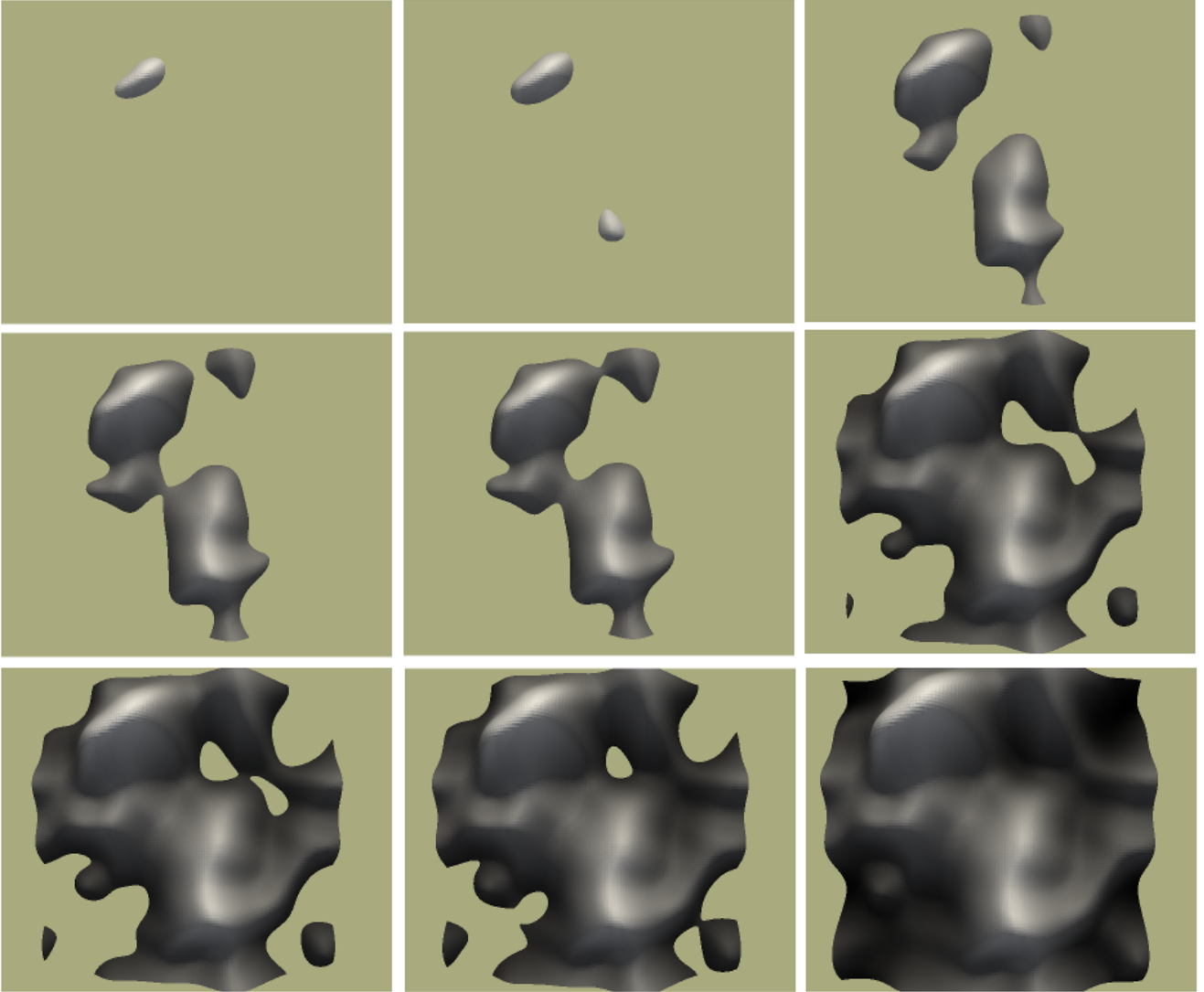
Figure 1. Topology and field singularity structure. The figure illustrates - from topleft to bottom right panel - the changing topology of the superlevel sets of a 2D random field as we lower the corresponding density threshold. The figure shows the regions of the topological space that are included in the superlevel set. Panel (a) starts with a single island. Panels (b) and (c) witness the birth of two more islands. In panel (d) two of the islands merge, so that two islands remain. In panel (e), there is another merger of two isolated islands, followed by the emergence of the first 1-dimensional hole or a loop in (f). It has the appearance of a lake surrounded by land. In panel (g), the loop splits into two, after which one of the loops get entirely filled up in panel (h) and disappears. In panel (i), all holes are filled up, with the superlevel set consisting of the entire topological space.

the fully continuous density field on the topological space, we need to define a strategy to infer the topological measures from the discrete point set.

Assuming the point sample is a representative and unbiased sample of the underlying continuous field, we may follow different strategies. Instrumental in this is the attempt to retain the optimal signal probing the underlying multiscale topology. The immediate implication for this is that we should refrain from the use of artificial filtering scales that beset so many conventional cosmological studies. Instead, we apply more natural filters that exploit fundamental concepts from computational geometry and computational topology (Okabe et al. 2000; Edelsbrunner & Harer 2010). These are based on the use of simplicial complexes - eg. the Delaunay tessellations that have been used in astronomical applications - that

form the natural format for the translation of a discrete point distribution into a continuous volume-filling field that retains all aspects of shape, morphology over the entire spectrum of scales.

A well-known strategy is the evaluation of the topological characteristics directly from the point sample distribution, on the basis of the distances between the sample points. A direct means of obtaining this information is via the construction of a simplicial complex. This is a geometric assembly of faces, edges, nodes and cells marking a discrete spatial map of the volume containing the point set. The edge lengths of such a complex would represent a selective sampling of the corresponding distance field. A well-known and topologically highly informative complex is that of *Alpha Shapes*. They are subsets of a Delaunay triangulation that describe the intuitive notion of the shape of a discrete point set.

They are one of the principal concepts from the field of Computational Topology (Dey et al. 1999; Rote & Vegter 2006; Zomorodian & Carlsson 2005). Introduced by Edelsbrunner and collaborators (Edelsbrunner et al. 1983; Edelsbrunner & Mücke 1994), these simplicial complexes constitute an ordered sequence of nested subsets of the Delaunay tessellation (Okabe et al. 2000; van de Weygaert & Icke 1989; van de Weygaert 1991; Edelsbrunner & Harer 2010). As they are homotopy equivalent to the distance field, they are an excellent tool for assessing the topological structure of a discrete point distribution. Instead of the cosmologically familiar filtration in terms of sublevel or superlevel sets defined by a density threshold, alpha shape topology is based on a distance filtration defined by the "scale" factor α. Our earlier preliminary studies of Betti number properties in a range of cosmological configurations, reported in (Eldering 2005; van de Weygaert et al. 2010; van de Weygaert et al. 2011), were based on the use of alpha shapes.

In this study we follow a different strategy, and evaluate the topological measures via a density value filtration of a reconstruction of the density field. To this end, we translate the discrete point distribution into a volume-filling density field reconstruction, using the Delaunay Tessellation Field Estimator or DTFE (Schaap & van de Weygaert 2000; van de Weygaert & Schaap 2009; Cautun & van de Weygaert 2011). It produces a piecewise linear continuous field of density values defined on the Delaunay triangulation generated by the distribution of sample points. The latter function as the vertices of the tessellation.

The core of our computational formalism is that of the subsequent homology calculation. We follow a technique that computes the homology measures directly from the continuous DTFE density field representation on the simplicial elements of the Delaunay tessellation K, ie. on the vertices, edges, triangular faces, and the tetrahedral cells. Instrumental in the algorithm are the density values at the vertices of the tessellation, and the increase or decrease in density towards the vertices to which they are connected in the tessellation. For a given density filtration, the calculation involves the determination of the boundary matrix (see Section 4, which identifies for each simplex in the superlevel filtration the simplices in its boundary. The reduction of the boundary matrix directly yields the birth-death pairs of the different p-dimensional persistence diagrams (see e.g. Edelsbrunner & Harer 2010; Bendich et al. 2010; Bauer et al. 2013).

A third computational aspects is the introduction of *persistence intensity maps*. These are designed for the practical purpose of evaluating and analyzing the intricate topological aspects of cosmological mass distributions. The intensity maps are continuous maps that represent an empirical probabilistic description of persistence diagrams. They are obtained via the averaging of persistence diagrams for a set of realizations of the same stochastic process, and are supposed to converge asymptotically to a stable average. Besides forming a continuous representation of persistence diagrams, they form a practical condensation of the topological character of a (density) field. They facilitate the comparison between different spatial distributions, outline and summarize their global topological properties while simultaneously allowing the detection of unique topological details that otherwise would have remained hidden. The latter would surface as the grid-wise difference between intensity map of a specific spatial mass distribution with respect to that for a set of reference morphologies.

1.7 This Study

The first two sections of this paper introduce the necessary mathematical concepts and background. Following a short discussion and definition of scalar fields and of Morse theory in Section 2, in the subsequent Section 3 we follow with a reasonably detailed introduction to the principal aspects of algebraic topology. This mathematical primer also includes an extensive and detailed presentation, in Section 4 of the computational machinery to compute persistence diagrams and Betti numbers. Before proceeding towards the topological analysis of clustered point distributions, Section 5 establishes the base reference. The section presents the results obtained in terms of Betti numbers and persistence diagrams for the random, featureless point distributions generated by a Poisson point process. Subsequently, Section 6 presents the results of the topological analysis of pure Voronoi element models, while Section 7 analyzes the topology of the multi-scale fractal Soneira-Peebles model (Soneira & Peebles 1978). Finally, an impression of the possible time evolution of the topology of the weblike cosmic mass distribution is obtained in Section 8, where we analyze the homology and persistence diagrams of elaborate and complex Voronoi evolution models. These are Voronoi clustering models that seek to emulate the morphological evolution of the cosmic web (van de Weygaert 2002). The concluding Section 9 presents a summary and discussion of our results and on the prospects for the application of homology and persistence measures for a quantitative characterization of the connectivity and morphological properties of the cosmic web.

2   SCALAR FIELDS AND MORSE THEORY

In this study we seek to analyze the homology of cosmological density fields. The mass distribution in the Universe is described by the density perturbation field,

$$f(x,t) = \frac{\rho(x,t) - \rho_u(t)}{\rho_u(t)}, \qquad (1)$$

which describes the fractional over- or under-density at position x with respect to the universal mean cosmological density $\rho_u(t)$.

2.1   Stochastic Random Fields

We start with the assumption that the cosmic density perturbation field is a realization of a stochastic random field. A *random field*, f, on a spatial volume assigns a value, $f(x)$, to each location, x, of that volume. The fields of interest are smooth and continuous [3]. The stochastic properties of a random field are defined by its *N-point joint probabilities*, where N can be any arbitrary positive integer. To denote them, we write $\mathbf{x} = (x_1, x_2, \cdots, x_N)$ for a vector of N points and $\mathbf{f} = (f_1, f_2, \ldots, f_N)$ for a vector of N field values. The joint probability is

$$\text{Prob}[f(x_1) = f_1, \ldots, f(x_N) = f_N] = \mathcal{P}_{\mathbf{X}}(\mathbf{f})\, d\mathbf{f}, \qquad (2)$$

which is the probability that the field f at the locations x_i has values in the range f_i to $f_i + df_i$, for each $1 \leqslant i \leqslant N$.

In cosmological circumstances, we use the *statistical cosmological principle*, which states that statistical properties of e.g. the

---

[3] In this section, the fields $f(x)$ may either be the raw unfiltered field or, without loss of generality, a filtered field $f_s(x)$. A filtered field is a convolution with a filter kernel $W(x, y)$, $f_s(x) = \int dy f(y) W(x, y)$.

cosmic density distribution in the Universe are uniform throughout the Universe. It means that the distribution functions and moments of fields are the same in each direction and at each location. The latter implies that ensemble averages depend only on one parameter, namely the distance between the points.

Important for the cosmological reality is the validity of the *ergodic principle*. The Universe is unique, and its density distribution is the only realization we have of the underlying probability distribution. The ergodic principle allows us to measure the value of ensemble averages on the basis of spatial averages. These will be equal to the expectations over an ensemble of Universes, something which is of key significance for the ability to test theoretical predictions for stochastic processes like the cosmic mass distribution with observational reality.

2.2   Superlevel Sets and Sublevel Sets

When assessing the mass distribution by a continuous density field, $f(x)$, a common practice is to study the sublevel or superlevel sets of the field smoothed on a scale R_s:

$$f_s(x) \quad = \quad \int f(y) W_s(y - x) \, dy, \qquad (3)$$

where $W_s(x - y)$ is the smoothing kernel. Writing $\mathbb{M}$ for the entire space, we define the *superlevel sets* of this field as the regions

$$\mathbb{M}_\nu = \{x \in \mathbb{M} \mid f_s(x) \geqslant \nu\} \qquad (4)$$

$$= f_s^{-1}[\nu, \infty). \qquad (5)$$

In other words, they are the regions where the smoothed density is greater than or equal to the threshold value.

The *sublevel set* is the complimentary topological space of the superlevel set. the *sublevel set* $\mathbb{M}^\nu$ is defined as

$$\mathbb{M}^\nu = \{x \in \mathbb{M} \mid f_s(x) \leqslant \nu\} \qquad (6)$$

$$= f_s^{-1}(-\infty, \nu]. \qquad (7)$$

Since both superlevel set and sublevel set are closed, they intersect in the *level set*

$$f^{-1}(\nu) = \mathbb{M}_\nu \cap \mathbb{M}^\nu. \qquad (8)$$

2.3   Filtrations

When addressing the topology of a mass or point distribution, a rich source of information is the topological structure of a filtration. Given a space $\mathbb{M}$, a *filtration* is a nested sequence of subspaces:

$$\emptyset = \mathbb{M}_0 \subseteq \mathbb{M}_1 \subseteq \ldots \subseteq \mathbb{M}_m = \mathbb{M}. \qquad (9)$$

The nature of the filtrations depends, amongst others, on the representation of the mass distribution. When assessing the topology of a scalar field, the filtration usually consists of the nested sequence of sublevel or superlevel sets. It is the evolving topology as we pass through the filtration seqencce which represents a rich source of information on the topological complexity of the field.

A typical example of superlevel sets of a density field is that shown in figure 2. It provides a telling illustration of a density-defined filtration of a weblike spatial pattern. It concerns a model of the cosmic web consisting exclusively of filaments. It shows a sequence of three growing superlevel sets of the weblike density field, along a sequence of decreasing density thresholds. The top panel corresponds to the highest density threshold. It reveals the high density regions that outline the underlying skeleton. The additional panels reveal complementary information on the mannner in
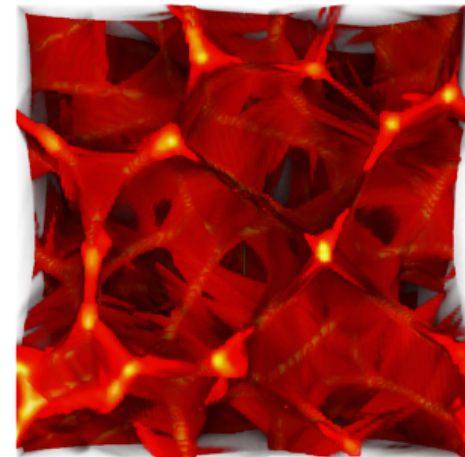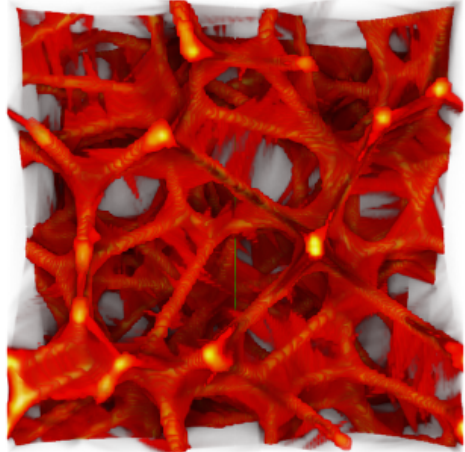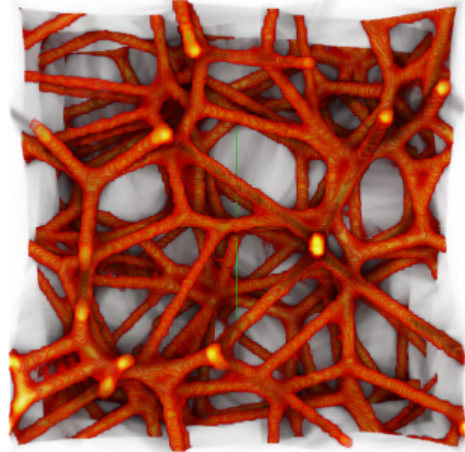

Figure 2. Density rendering of the superlevel set of the pure filamentary models. From top to bottom: three snapshots for growing superlevel sets.

which matter has distributed itself over the various structural components, revealing how the lower density mass elements connect up and fill in the intersticial regions of the network.

The illustration shows how the sequence of filtration steps establish the connectivity of the cosmic mass distribution, and entails its topological structure.

2.4 Piecewise Linear Scalar Fields

In many practical circumstances, whether it concerns the spatial distribution of galaxies in redshift surveys or particles in cosmological N-body simulations, we are dealing with datasets consisting of discrete particle positions.

There are various ways in which the topology of such a discrete particle dataset can be analyzed. One option is to define a filtration on the point distribution itself. The most direct way to achieve this is that via a simplicial complex generated by the point distribution. Well-known examples are that of the alpha-complex and the Cech complex (see Edelsbrunner & Harer 2010), invoking the distance function and a corresponding distance parameter to define the filtration.

In our study we follow a different approach. The topological analysis in our study is based on a density value based filtration of a piecewise linear density field. The latter is computed from the discrete particle distribution itself. The usual strategy for this is to compute a triangulation on the given discrete particle set. The density function is first calculated on the vertices of this triangulation, and subsequently extrapolated to the higher dimensional simplices, yielding a piece-wise linear function. More details on this can be found in the subsection on piece-wise linear functions, as well as Section 4. The filtration consists of density superlevel sets.

The determination of a piecewise linear density field from a discrete particle distribution involves a few key steps. The first step involves an estimate of the density at each of the sample points. Usually, the particles define the point sample, but in principle one may define alternatives. The second step involves the determination of a tessellation on the basis of the point sample. In each tetrahedron of the tessellation, the gradient can be uniquely determined from its four vertices.

For a sample of N points, with density value estimates $f(x_j)$ ($j = 1, 2, \ldots, N$), the density value $f(x)$ at a location x is uniquely determined from the density gradient of the tetrahedron in which it is located, and the density value at one of its vertices, x_i,

$$f(x) = f(x_i) + \nabla f \cdot (x - x_i). \tag{10}$$

One key element of a procedure to construct a linear piecewise density field is the nature of the estimate of the density at each sample point. A second key element is the nature of the triangulation. For our results, In most of our results, we use the Delaunay Tessellation Field Estimator, DTFE (Schaap & van de Weygaert 2000; van de Weygaert & Schaap 2009; Cautun & van de Weygaert 2011). It is based on local density estimates. The density at a particular vertex is the inverse of the volume of the delaunay star associated with it. The density is then interpolated to higher dimensional simplices, to yield a piece-wise linear field.

2.5 Morse Theory

In Morse theory, we consider a compact topological space $\mathbb{M}$, and a generic smooth function on this topological space. In the context

of this paper, the topological space is the 3-torus [4] and the function is a density distribution, $f : \mathbb{M} \to \mathbb{R}$. Assuming f is smooth, we can take derivatives, and we call a point $x \in \mathbb{M}$ *critical* if all partial derivatives vanish, i.e.,

$$\nabla f|_x = 0. \tag{11}$$

Correspondingly, $f(x)$ is a *critical value* of the function. All points of $\mathbb{M}$ that are not critical are *regular points*, and all values in $\mathbb{R}$ that are not the function value of critical points are *regular values*. Finally, we call f *generic* if all critical points are non-degenerate in the sense that they have invertible Hessians, which is defined as the matrix of the partial double derivatives

$$H_{ij} = \left(\frac{\partial f}{\partial x_i \partial x_j} \right)_{i=1,\ldots,3; j=1,\ldots,3}, \tag{12}$$

restricting to a 3-dimensional space. In this case, critical points are isolated from each other, and since $\mathbb{M}$ is compact, we have only finitely many critical points and therefore only finitely many critical values. The *index* of a non-degenerate critical point is the number of negative eigenvalues of the Hessian. Since $\mathbb{M}$ is 3-dimensional, we have 3-by-3 Hessians and therefore only four possibilities for the index. A *minimum* of f has index 0, a *maximum* has index 3, and there are two types of *saddles*, with index 1 and 2.

A major result of Morse theory states that the topology of a space changes only when the level set passes a critical point of the function. The change in topology is dictated by the index of the critical point. The significance of the critical points and their indices becomes apparent when we look at the sequence of growing superlevel sets: $\mathbb{M}_\nu = f^{-1}[\nu, \infty)$, for $0 \leqslant \nu < \infty$. If $\nu > \mu$ are regular values for which $[\mu, \nu]$ contains no critical value then $\mathbb{M}_\nu$ and $\mathbb{M}_\mu$ are topologically the same, the second obtained from the first by diffeomorphic thickening all around. If $[\mu, \nu]$ contains the critical value of exactly one critical point, x, then the difference between the two superlevel sets depends only on the index of x. If x has index 3 then $\mathbb{M}_\mu$ has one more component than $\mathbb{M}_\nu$, and that component is a topological ball. If x has index 2, then $\mathbb{M}_\mu$ can be obtained from $\mathbb{M}_\nu$ by attaching an arc at its two endpoints and thickening all around. This extra arc can have one of two effects on the homology of the superlevel set. If its endpoints belong to different components of $\mathbb{M}_\nu$, then $\mathbb{M}_\mu$ has one less component, while otherwise $\mathbb{M}_\mu$ has one more loop. If x has index 1, then $\mathbb{M}_\mu$ can be obtained from $\mathbb{M}_\nu$ by attaching a disk, which has again one of two effects on the homology groups. Finally, if x has index 0 then $\mathbb{M}_\mu$ is obtained by attaching a ball. In all cases but one, this ball fills a void, the exception being the last ball that is attached when we pass the global minimum of f. At this time, the superlevel set is completed to $\mathbb{M}_\mu = \mathbb{M}$.

3 TOPOLOGY

In this section, we introduce the topological concepts we use to analyze particle distributions. The main new methods for cosmological

---

[4] In the cosmological context, the data is usually specified in a cubic box. Gluing opposite ends of the cube converts it into a 3-torus. This has the advantage of converting the data into a periodic form. This is reasonable, also from the assumptions of the cosmological principle, stating that there are no preferred locations in the Universe. Converting the data into a periodic form mimics this principle.
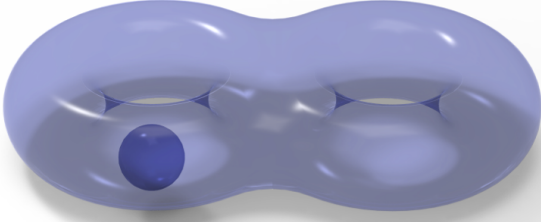
Figure 3. Running example of nontrivial topology: a solid double-torus containing an empty bubble. The boundary surface of this double-donut with small void inside consists of two parts, a double-torus on the outside and a sphere encapsulating the bubble. For further explanation see sect. 3.

applications are Betti numbers and persistence, which we will relate to the more traditional notions of Minkowski functionals, Euler characteristic, and genus.

3.1 Euler Characteristic and Genus

Let us have a solid body $\mathbb{M}$. Suppose now that we have the boundary of $\mathbb{M}$ triangulated, using v vertices, e edges, and t triangles. The vertices, edges triangles and tetrahedra are also referred to as *simplices*. A vertex is a 0-dimensional simplex, an edge is a 1-dimensional simplex, a triangle is a 2-dimensional simplex, and a tetrahedron is a 3-dimensional simplex. Figure 3 presents an illustration of simplices in dimensions up to 3.

Named after Leonhard Euler (Euler 1758), the *Euler characteristic* of the surface — traditionally denoted as χ — is the alternating sum of the number of simplices:

$$\chi = v - e + t. \tag{13}$$

It does not depend on the triangulation, only on the surface. For example, we can triangulate the sphere with 4 vertices, 6 edges, and 4 triangles, like the boundary of the tetrahedron, which gives $\chi = 4 - 6 + 4 = 2$. Alternatively, we may triangulate it with 6 vertices, 12 edges, and 8 triangles, like the boundary of the octahedron, which again gives $\chi = 6 - 12 + 8 = 2$.

Generalizing this to a orientable connected closed surface S [5], with $h \geqslant 0$ handles the Euler characteristic is equal to 2 minus twice the number of handles, is $\chi = 2 - 2h$. For example, the sphere has $\chi = 2$ and the torus has $\chi = 0$. If the boundary of $\mathbb{M}_v$ consists of k components with a total of h holes, then we have $\chi = 2(k - h)$. To make this more concrete, we formalize the number of holes of a closed, connected surface to its *genus*, denoted as $g = h$. It is defined as the maximum number of disjoint closed curves we can draw on the surface such that cutting along them leaves the surface in a single connected piece. For example, for a sphere we have $g = 0$, and for a torus we have $g = 1$. If we now drop the assumption that the surface is connected, we get the Euler characteristic and genus by taking the sum over all components. Since $\chi_i = 2 - 2g_i$ for the i-th component, we have

---

[5] An *orientable* surface in Euclidean space is a surface for which it is possible to make a consistent choice of surface normal vector at every point. A *closed* surface is a surface which is compact and without boundary.

$$\chi = \sum_{i=1}^{k} \chi_i = \sum_{i=1}^{k} (2 - 2g_i) = 2k - 2g. \tag{14}$$

We see that a minimum amount of topological information is needed to translate between Euler characteristic and genus. This is different from what the cosmologists have traditionally called the genus, which is defined as $\tilde{g} = -\frac{1}{2}\chi$ (Gott et al. 1986; Hamilton et al. 1986). Relating the two notions, we get $g = k + \tilde{g}$. We will abandon both in this paper, $\tilde{g}$ because it is redundant, and g because it is limited to surfaces. Indeed, the Euler characteristic can also be defined for a 3-dimensional body, taking the alternating sum of the simplices used in a triangulation, while the genus has no satisfactory generalization beyond 2-dimensional surfaces.

3.2 Minkowski Functionals

Suppose we have a solid body, $\mathbb{M}$, whose boundary is a smoothly embedded surface in $\mathbb{R}^3$. This surface may be a sphere or have holes, like the torus, and it may consist of one or several connected components, each with its own holes. Similarly, we do not require that $\mathbb{M}$ is connected. Write $\mathbb{M}^r$ for the set of points at distance r or less from $\mathbb{M}$. For small values of r, the boundary of $\mathbb{M}^r$ will be smoothly embedded in $\mathbb{R}^3$, but as r grows, it will develop singularities and self-intersections. Before this happens, the volume of $\mathbb{M}^r$ can be written as a degree-3 polynomial in r,

$$\text{vol}\,\mathbb{M}^r = Q_0 + Q_1 r + Q_2 r^2 + Q_3 r^3. \tag{15}$$

The Q_i are known as the *Minkowski functionals* of $\mathbb{M}$, which are important concepts in integral geometry. Minkowski functionals were first introduced as measures of the spatial cosmic mass distribution by Mecke et al. (1994b) and have become an important measure of clustering of mass and galaxies (Schmalzing & Buchert 1997; Schmalzing et al. 1999; Sahni et al. 1998).

In terms of their interpration in the 3-dimensional context, following Equation (15), we see that Q_0 is the volume of $\mathbb{M}$, Q_1 is the area of its boundary, Q_2 is the total mean curvature, and Q_3 is one third of the total Gaussian curvature of the boundary. These interpretations suggest that the Minkowski functionals are essentially geometric in nature, and they are, but there are strong connections to topological concepts as well. The key connection is established via the Euler characteristic.

3.3 Geometry and Topology: Gauss–Bonnet Theorem

The key connection between the geometric Minkowski functionals and topology is established via the Euler characteristic, $\chi(S)$, of a surface S. The connection between the topological characteristics of a space and its geometrical properties is stated by the famous Gauss–Bonnet theorem. For a connected closed surface S in $\mathbb{R}^3$, the Gauss–Bonnet theorem asserts that the total Gaussian curvature is 2π times the Euler characteristic $\chi(S)$,

$$\chi(S) = \frac{1}{2\pi} \oint \left(\frac{1}{R_1 R_2} \right) dS, \tag{16}$$

where R_1 and R_2 are the principal radii of curvature at each point of the surface. Note that the Gauss–Bonnet theorem only holds for smooth surfaces, meaning surfaces for which at least the second derivative is well-defined. For the situation sketched above, a boundary of space $\mathbb{M}$ consisting of k components with a total of h holes, it tells that the total Gaussian curvature will be equal to

$4\pi(k - h)$. For example, the Gaussian curvature of a sphere with radius r is $1/r^2$ at every point. Multiplying with the area, which is $4\pi r^2$, we get the total Gaussian curvature equal to 4π, which is independent of the radius. This agrees with $\chi = 4\pi(k - h)$ given above since $k - h = 1$ in this case.

The Gauss–Bonnet theorem (eq. 16) underlines the key position of the Euler characteristic at the core of the topological and geometric characterization of topological spaces. The Euler characteristic establishes profound and perhaps even surprising links between seemingly widely different areas of mathematics. While in simplicial topology Euler's polyhdron formula states that it is the alternating sum of the number of k-dimensional simplices of a simplicial complex (eq. 13), its role in *algebraic topology* as the alternating sum of Betti numbers is expressed by the Euler–Poincaré formula (see eq. 17 in the next subsection). Even more intricate is the connection that it establishes between these topological aspects and the singularity structure of a field, which is the realm of *differential topology*. In particular interesting is the relation established by Morse theory of the Euler characteristic being equal to the alternating sum of the number of different field singularities, ie. of maxima, minima and saddle points. Finally, its significance in *integral geometry* is elucidated via Crofton's formula, which establishes the fact that Minkowski functionals are integrals over the Euler characteristic of affine cross-sections.

3.4 Homology and Betti Numbers

While the Euler characteristic can distinguish between connected, closed surfaces in $\mathbb{R}^3$, it has no discriminative power if applied to 3-manifolds, which is the most direct generalization of surfaces to the next higher dimension. Indeed, Poincaré duality implies $\chi = 0$ for all 3-manifolds. Fortunately, we can write the Euler characteristic as an alternating sum of more descriptive topological invariants named after Enrico Betti (Betti 1871). To introduce them, we find it convenient to generalize the space $\mathbb{M}$ by dropping most limitations, such as that it be embedded or even embeddable in $\mathbb{R}^3$. Letting the intrinsic dimension of $\mathbb{M}$ be d, we get $d + 1$ possibly non-zero *Betti numbers*, which traditionally are denotes as $\beta_0, \beta_1, \ldots, \beta_d$. The relationship to the Euler characteristic is give by the Euler–Poincaré Formula:

$$\chi = \beta_0 - \beta_1 + \beta_2 - \ldots (-1)^d \beta_d. \qquad (17)$$

This relation holds in great generality, requiring only a triangulation of the space, and even this limitation can sometimes be lifted. In this paper, we only consider subspaces of the 3-torus, $\mathbb{M}$. For this case, only $\beta_0, \beta_1, \beta_2$, and β_3 are possibly non-zero, and we have $\beta_3 \neq 0$ only if $\mathbb{M}$ is equal to the 3-torus, in which case $\beta_3 = 1$. The first three Betti numbers have intuitive interpretations: β_0 is the number of *components*, β_1 is the number of *loops*, and β_2 is the number of *shells* in $\mathbb{M}$. Often, it is convenient to consider the complement of $\mathbb{M}$, which shows $\beta_0 - 1$ *gaps* between the components, β_1 *tunnels* going through the loops, and β_2 *voids* enclosed by the shells.

A formal definition of the Betti numbers requires the algebraic notion of a homology group. While a serious discussion of this topic is beyond the scope of this paper, we provide a simplified exposition and refer to texts in the algebraic topology literature for details (see e.g. Munkres 1984).

For simplicity, we assume a triangulated space and we use the coefficients 0 and 1 and addition, modulo 2. A *p-chain* is a formal sum of the *p*-simplices in the triangulation, which we may interpret as a subset of all *p*-simplices, namely those with coefficients

1. The *sum* of two *p*-chains is again a *p*-chain. Interpreted as sets, the sum is the symmetric difference of the two sets. Note that each *p*-simplex has $p + 1$ $(p - 1)$-simplices as faces. The *boundary* of the *p-chain* is then the sum of the boundaries of all *p*-simplices in the chain. Equivalently, it is the set of $(p - 1)$-simplices that belong to an odd number of *p*-simplices in the chain. We call the *p*-chain a *p-cycle* if it is the boundary of a $(p + 1)$-chain. Importantly, every *p*-boundary is a *p*-cycle. The reason is simply that the boundaries of the $(p - 1)$-simplices in the boundary of a *p*-simplex contain all $(p - 2)$-simplices twice, meaning the boundary of the boundary is necessarily empty. To get homology, we still need to form *classes*, which we do by not distinguishing between two *p*-cycles that together form the boundary of a $(p + 1)$-chain.

To get the group structure, we add *p*-cycles by taking their symmetric difference or, equivalently, by adding simplices modulo 2. Homology classes can now be added simply by adding representative *p*-cycles and taking the class that contains the sum. The collection of classes together with this group structure is the *p-th homology group*, which is traditionally denoted as H_p. Finally, the *p-th Betti number* is the rank of this group, and since we use modulo 2 arithmetic to add, this rank is the binary logarithm of the order: $\beta_p = \log_2 |H_p|$. We note that modulo 2 arithmetic has multiplicative inverses and therefore forms what in algebra is called a *field* [6]. For example, arithmetic with integers is not a field. Whenever we use a field to construct homology groups, we get vector spaces. In particular, the groups H_p defined above are vector spaces, and the β_p are their dimensions, as defined in standard linear algebra.

In our study, we forward Betti numbers for the characterization of the topological aspects of the cosmic mass distribution.

3.5 Running Example

We begin with an example, which we use to illustrate the geometric and topological concepts, ahead of formally defining them. For this purpose, let $\mathbb{M}$ be a solid double-torus with an empty bubble, that is: a double-donut with a small void inside; see Figure 5. Its boundary, denoted as $\partial\mathbb{M}$ consists of two surfaces: a double-torus on the outside and a sphere bounding the bubble.

The *Minkowski functionals* are the volume of $\mathbb{M}$, the area, the total mean curvature, and the total Gaussian curvature of $\partial\mathbb{M}$. These are geometric properties, but they are not independent of the purely topological concepts we will introduce next.

The *Euler characteristic* is the alternating sum of the number of simplices of different dimensions needed to triangulate a space. Applied to $\partial\mathbb{M}$, the number of vertices minus the number of edges plus the number of triangles needed to triangulate the double-torus gives -2, and for the sphere we get $+2$. It follows that the Euler characteristic of $\partial\mathbb{M}$ is $\chi = 0$. There are many other 2-dimensional topological spaces that have the same Euler characteristic, the torus being one, the union of two tori being another.

Indeed, the total Gaussian curvature of the sphere is 4π, no matter how large it is, and the Euler chatacteristic of the same is 2. The *genus* of $\partial\mathbb{M}$ is 2, namely 2 for the double-torus plus 0 for the sphere. For a connected closed surface, the genus equals 1 minus half the Euler characteristic. More generally, the genus of a 2-manifold that is the union of disjoint closed surfaces is therefore

---

[6] The algebraic concept of field is not to be confused with the physical notion of (scalar density) field that also plays a prominent role in this paper.
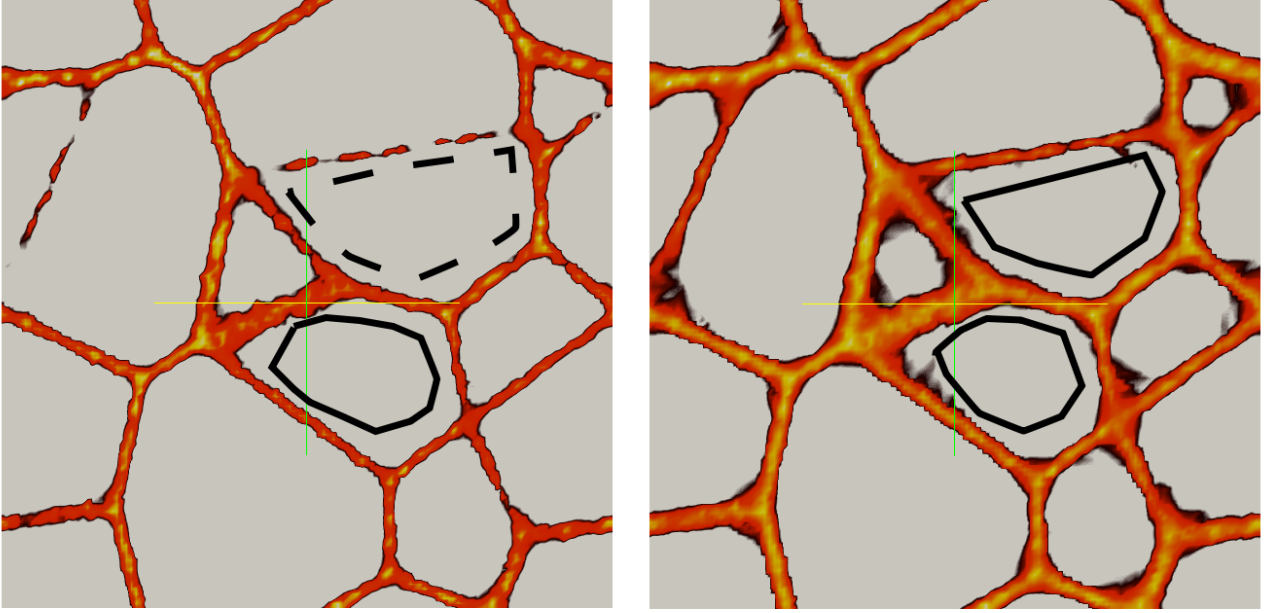
Figure 4. Chains and Cycles. Density rendering of the superlevel set of a 2-dimensional cross section of a Voronoi wall model. The lefthand frame corresponds to a higher density threshold value than that in the righthand frame. Particularly attention concerns the cells in which we have marked the outline by black lines. For a high threshold value, the superlevel structure traced by the dashed closed curve does not form a loop: the multiple broken segments are *chains*. At a lower threshold value, the superlevel structure becomes continuous, and individual segments merge together to form a loop: a 1-dimensional *cycle*.

$$g = \sum_i g_i = \sum_i \left(1 - \frac{\chi_i}{2}\right) = \#\text{components} - \left(\frac{\chi}{2}\right), \quad (18)$$

where we write χ_i and g_i for the Euler characteristic and the genus of the i-th component. The reader may check that this relation holds for $\partial\mathbb{M}$. We get a refinement of the concepts by introducing *Betti numbers*. Formally, they are ranks of homology groups, one for each dimension (more on homology and homology groups later). We have

$$\begin{aligned}
\beta_0 &= \#\text{components}, \\
\beta_1 &= \#\text{independent loops}, \quad (19) \\
\beta_2 &= \#\text{independent closed surfaces}.
\end{aligned}$$

For $\partial\mathbb{M}$, we have $\beta_0 = 2, \beta_1 = 4, \beta_2 = 2$. Indeed, we have two components and two closed surfaces: the double-torus and the sphere. To see the four loops, draw one around each hole of the double-torus and another one around each handle. We get the Euler characteristic by taking the alternating sum: $\chi = \beta_0 - \beta_1 + \beta_2$, which for $\partial\mathbb{M}$ gives 0, as required.

Suppose now that $\mathbb{M}$ is the portion of the Universe at which the local density exceeds some threshold, ν. What if we decrease ν by some small but positive amount? Decreasing the threshold enlarges the portion at which the density threshold is exceeded. It may be that the bubble fills up. Assuming that nothing else changes, $\partial\mathbb{M}$ is now a double-torus, with $\beta_0 = 1, \beta_1 = 4, \beta = 1$. The sphere and the bubble have gone.
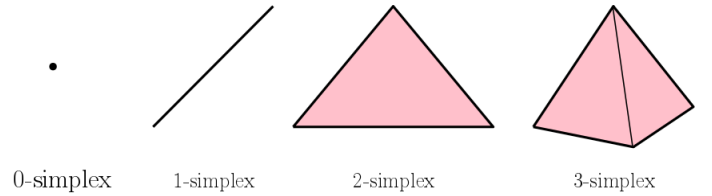

Figure 5. From left to right: 0, 1-, 2- and 3- simplex.

3.6 Persistent Homology

In Morse theory, we learned that passing a critical point either increases the rank of a homology group by one, or it decreases the rank of another group by one. Equivalently, it gives birth to a generator of one group or death to a generator of another group. Our goal is to pair up births with deaths such that we can talk about the subsequence in the filtration over which a homology class exists. This is precisely what persistent homology accomplishes.

Recall that between two consecutive critical values, the homology of the superlevel sets is constant. It therefore suffices to pick one regular value within each such interval. Writing $r_0 > r_1 > \ldots > r_n$ for these regular values, this induces a sequence of inclusions

$$\mathbb{M}_0 \to \mathbb{M}_1 \to \cdots \to \mathbb{M}_i \to \cdots \to \mathbb{M}_n, \quad (20)$$

where $\mathbb{M}_i$ is the manifold defined by the superlevel set r_i.

The inclusion $\mathbb{M}_{i-1} \to \mathbb{M}_i$ maps a p-cycle in $\mathbb{M}_{i-1}$ to a p-cycle in $\mathbb{M}_i$, and a p-boundary in $\mathbb{M}_{i-1}$ to a p-boundary in $\mathbb{M}_i$. Therefore, it induces a map $H_p(\mathbb{M}_i) \to H_p(\mathbb{M}_{i+1})$, which is a homomorphism since it preserves the group structure. So we have d+1 sequences

$$H_p(\mathbb{M}_0) \to H_p(\mathbb{M}_1) \to \cdots \to H_p(\mathbb{M}_n), \quad (21)$$

for $p = 0, 1, \ldots, d$.

Assuming coefficients in a field [7], as before, we have a sequence of vector spaces with linear maps between them. These maps connect the groups by telling us where to find the cycles of a homology group within later homology groups. Sometimes, there are new cycles that cannot be found as images of incoming maps, and sometimes classes merge to form larger classes, which happens when we get chains that further wash out the difference between cycles.

To simplify notation, we will assume a particular dimension, p, so that we can suppress the subscript. Instead, we write $H_i = H_p(\mathbb{M}_i)$, effectively indexing the homology groups with the position along the filtration. We can now be specific about the persistence of homology classes. Letting γ be a class in H_i, we say γ is *born* at H_i and *dies entering H_j* if

- γ is not in the image of H_{i-1} in H_i;
- the image of γ is not in the image of H_{i-1} in H_{j-1}, but it is in the image of H_{i-1} in H_j.

Letting $r_{i-1} > v_i > r_i$ and $r_{j-1} > v_j > r_j$ be the critical values in the relevant intervals, we represent γ by (v_i, v_j), which we call a *birth-death pair*. Furthermore, we call $\text{pers}(\gamma) = v_i - v_j$ the *persistence* of γ, but also of its birth-death pair.

To avoid any misunderstanding, we note that there is an entire coset of homology classes that are born and die together with γ, and all these classes are represented by the same birth-death pair. Calling the image of H_i in H_{j-1} a *persistent homology group*, we note that its rank is equal to the number of birth-death pairs (v_b, v_d) that satisfy $v_b \geqslant v_i > v_j \geqslant v_d$. They represent the classes that are born at or before H_i and that die entering H_j or later.

Finally, for whom this description of persistence and homology is not immediately clear, we refer to Section 4.4 for a concrete example of filtration and persistent homology.

3.7 Intensity Maps

This paper concerns itself with the topology of stochastic point processes, and density field computed on them. In the context of the Universe, both the cosmic microwave background and the density distribution in the Universe are examples of spatial stochastic processes. It is a universal property of stochastic processes that the expectation value of the quantities defined on them converge over many realizations. Our conjecture is that this must also be true for the birth-death events, as reflected in the persistence diagrams, if averaged over many realizations. While a rigorous attempt at deriving a probabilistic and statistical description of persistence topology is beyond the scope of this paper, we provide an emperical description and test, as proof of the hypothesis, by introducing the intensity maps.

We are interested in the statistical description of persistence diagrams, as an average over many realization, of the stochastic process f. To this end, we construct the *intensity map*, which is the function $p : \mathbb{R}^2 \to \mathbb{R}$ in the *mean density-persistence* plane [8],

whose integral over every region $R \subset \mathbb{R}^2$ is the expected number of points in R. Let $\langle N_{tot} \rangle$ be representative of the *total intensity* of the map. We discretize the intensity map into a number of regular grid-cells in the plane, and define the bin-wise intensity, for the grid-cell (i, j) as

$$I_{ij} = \frac{\langle N_{ij} \rangle}{\langle N_{tot} \rangle}, \tag{22}$$

where, $\langle N_{ij} \rangle$ is the expected intensity in the grid-cell (i, j), and $\langle N_{tot} \rangle$ is the expected total intensity, over many realizations of the same random experiment.

The total *intensity* of the maps is proportional to the average number of total dots in the persistence diagrams. For each grid cell, the intensity function represents the fraction of the total intensity of the map. Since the intensity in each bin is normalized by the total intensity of the map, the integral of the intensity function over $\mathbb{R}^2$ always evaluates to 1, irrespective of the model in question. In the limit of the size of the grid-cells going to zero, the discretized intensity function approximates the probability density function. At this point, we only have emperical evidence that if f arises from a stochastic process and is tame (all the derivatives well defined), the intensity maps are well defined . As we will show shortly, the intensity maps are highly sensitive to the parameters of the model, and capture local variations in topology across the whole range of function value. As such, we propose their use to characterize and discriminate between various models.

4 COMPUTATION

The geometric and topological concepts outlined in Sections 2 and 3 have all matured to a stage at which we have fast software to run on simulated and observed data. In this section, we describe the principles of these algorithms, and we provide sufficient information for the reader to understand the connection between the mathematics, the data, and the computed results.

The computational framework of our study involves three components. The first component concerns the definition and calculation of the density field on which we apply the field's filtration. This is described in Section 4.1. A directly related issue is the representation of the density field in the homology calculation, ie. whether we retain its representation by density estimates at the original sampling points or whether we evaluate it on the basis of a density image on a regular grid. The second component of the computational pipeline, is the algorithm used for computing persistent homology. This involves building a filtration, described in Section 4.2, and the subsequent computation of persistent homology on this filtration, which is described in Section 4.3. The third aspect concerns the representation of the results of the homology and persient homology computation. The principal products consist of *intensity maps* and *Betti numbers* of the analyzed samples, which form the visual representation and summary of persistent homology and homology. The construction of intensity maps is described in detail in Section 3.7, as well as Section 4.3.

4.1 Density Reconstruction from Point Sample

We use DTFE (Schaap & van de Weygaert 2000; van de Weygaert & Schaap 2009; Cautun & van de Weygaert 2011) to construct a piecewise linear scalar-valued density field from a particle distribution. The DTFE formalism involves the computation of the Delaunay tessellation of the particles in $\mathbb{M}$, the determination of tessel-

---

[7] The betti numbers might depend on the choice of the field. For example, β_2 of the projective plane is 1, if the field is Z_2, and 0 for the field of rational numbers. However, such considerations do not apply if the surfaces are orientable, which is the case that we deal with.

[8] This is a plane defined by the mean-density of the features on the horizontal axis, which is the mean of birth and death values of the features. The vertical axis is defined by the persistence value of the features.

Model	# particles	# simplices	Del. (s)	Pers. (s)
Poisson	500,000	14,532,164	10.15	6414.16
Cluster	262,144	7,491,308	81.48	12.58
Filament	262,144	7,346,712	77.76	402.36
Wall	262,144	7,345,520	5.26	555.46
Voronoi Kinematic Stage 3	262,144	7,409,364	5.93	125.33
Soneira–Peebles $\zeta = 9.0$	531,441	14,300,836	162.42	168.15

Table 1. Parameters of computation for the various models described in this paper. All computations are performed on an Intel(R) Xeon(R) CPU @ 2.00GHz. Columns 1 & 2 present the models described in the later sections, and the number of particles used for the computation. Column 3 gives the total number of simplices of the Delaunay tessellation. Columns 4 & 5 give the time required to compute the tessellation and persistence respectively, in seconds.

lation based density estimates, and the subsequent piecewise linear interpolation of the density values at the Delaunay vertices, ie. the sample points, to the higher dimensional simplices, yielding a field $f : \mathbb{M} \to \mathbb{R}$. Figure 3 presents an illustration of simplices in spatial dimensions up to 3.

For the calculation of the Delaunay tessellation, we use software in the CGAL library. We use the 3-torus option of CGAL, which is the periodic form of the original data set in a cubic box obtained by identifying opposite faces of the box.

In a second step, we compute the DTFE density value for each vertex, u, of the Delaunay tessellation. The DTFE density value at the vertices is the inverse of the volume of its *star*. The star consists of all simplices that contain u as a vertex (see Figure 6 for an illustration), and we assign one over this volume as the density value to u. Finally, we use piece-wise linear interpolation to define $f : \mathbb{M} \to \mathbb{R}$. In the context of our study, we follow this *Raw DTFE sampling* strategy. The particular nature of the discretely sampled density field involves a complication. Because the number density of the sample points represents a measure of the value of the density field itself, the DTFE density field has a much higher spatial resolution in high density regions than in low density regions. This might be a source of a strong bias in the retrieved topological information, given that most of this will focus on the topological structure of the high-density regions.

To alleviate a density bias towards the highly sampled regions, one may invoke a range of strategies. One option is to sample the density field on a regular grid. In other words, to create an image of the DTFE density field reconstruction. It has the advantage of representing a uniformly sampled density field, with a uniform spatial resolution dictated by the voxel size of the image. However, following this option involves the loss of resolution in the high density regions. On the other hand, it retains the DTFE advantage of sampling the low density - void - regions well. Dependent on the region of interest one may therefore choose to use the raw DTFE method or the grid-sampled one. Additionally though, it is important to note that the homology analysis a gridbased image involves a few extra complications, the details of which are most extensively discussed in the follow-up study analyzing the homology and persistence of Gaussian random fields (see Pranav et. al. 2016a,b).

Another strategy to moderate the bias towards high-density regions is to use the singularity structure of the piecewise linear density field, and use the persistence of singularity pairs to remove insignificant topological features. This natural feature-based smoothing of the density field has been described extensively and has been applied in studies of cosmic structures by Sousbie (2011) and by Shivashankar et al. (2016).

Table 1 presents the noteworthy parameters of computations for a single realization of the different models used in the results section of this paper. Naming the models in Column 1, we see the number of particles and simplices in the Delaunay tessellation in Columns 2 and 3 (also see Okabe et al. 2000; van de Weygaert 1994), and the number of seconds needed to compute the Delaunay tessellation and the persistence pairs in Columns 4 and 5. Apparently, the number of particles is not strongly correlated with the time it takes to construct the Delaunay tessellation. Indeed, the algorithm is also sensitive to other parameters — such as the number of simplices in the final simplicial complex or ever constructed and destroyed during the runtime of the algorithm — that depend on how the particles are distributed in space.

4.2 Critical Values and Filtration

As mentioned in the paragraph on Morse theory, the superlevel set does not change topology as long as v does not pass a critical value of the function, and this is also true for piecewise linear functions, except that we need to adjust the concept of critical point. Here we do the obvious, looking at how f varies in the *link*, of a vertex. The link consists of all faces of simplices in the star, that do not themselves belong to the star (Edelsbrunner & Harer 2010, Chapter VI). Indeed, the topology can change only when v passes the value of a vertex, so it suffices to consider only one (regular) value between any two contiguous vertex values. To describe this, we let n be the number of vertices in the tessellation, and we assume $v_i = f(u_i) < v_{i+1} = f(u_{i+1})$ for $1 \leqslant i < n$.[9] We thus consider superlevel sets at the regular values in the sequence

$$r_0 > v_1 > r_1 > v_2 > \ldots > v_n > r_n.$$

Constructing these superlevel sets and computing their homology individually would be impractical for the data-sets we study in this paper. Fortunately, there are short-cuts we can take that speed up the computations while having no effect on the computed results. The first short-cut is based on the observation that $\mathbb{M}_v$ has the same homotopy type as the subcomplex K_v of the tessellation K of $\mathbb{M}$ that consists of all vertices with $f(u_i) \geqslant v$ and all simplices connecting them. There is a convenient alternative description of K_v. Define the *upper star* of a vertex u as the collection of simplices in the star for which u is the vertex with smallest density value (see Figure 6 for the upper star of a regular vertex, a 1-saddle, a 2-saddle an a maximum). Then K_v is the union of the upper stars of all vertices with $f(u_i) \geqslant v$. This description is computational convenient because it tells us that $K_{r_{i+1}}$ can be obtained from K_{r_i} simply by adding the simplices in the upper star of u_{i+1}. We say the superlevel sets can be computed *incrementally*, and we will be careful to follow this paradigm in every step of our computational pipeline. This

---

[9] It is unlikely that the estimated density values at two vertices are the same, and if they are, we can pretend they are different, eg. by simulating a tiny perturbation that agrees with the ordering of the vertices by index; see eg. (Edelsbrunner 2001, Section I.4).
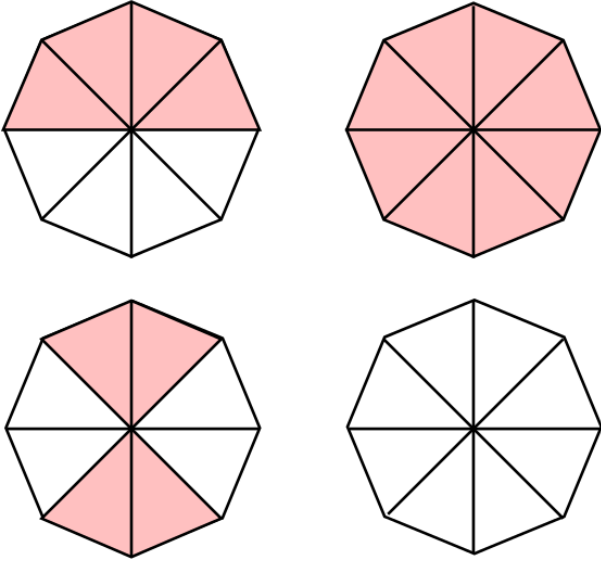
Figure 6. Figure illustrating the upper star of a regular vertex, minimum, saddle and maximum, respectively in top-left, top-right, bottom-left, bottom-right panels. The star of a vertex is consists of all the simplices incident to it. The shaded simplices in pink have a function value higher than the vertex.

incremental construction of the superlevel sets is equivalent to constructing the upper-star filtration, which is an essential pre-cursor to computing persistence homology.

To give a visual impression of superlevel sets of tessellations constructed in the practical circumstances, Figure 7 presents an illustration of the growing superlevel sets of a filtration of a simplicial complex constructed on a pointset obtained from a typical cosmological simulation.

4.3 Persistent Homology

Next, we sketch the algorithm that computes the persistent homology of the sequence of superlevel sets. We begin with a linear ordering of the simplices in K that contains all K_v as prefixes. To describe it, let $u_i = \sigma_{j_i}, \sigma_{j_i+1}, \ldots, \sigma_{j_{i+1}-1}$ be the simplices in the upper star of u_i, sorted in increasing order of dimension. Setting $j_1 = 1$ and $m = j_{n+1} - 1$, this linear ordering of the simplices is $\sigma_1, \sigma_2, \ldots, \sigma_m$. It has the property that each simplex is preceded by its faces, which implies that every prefix, $K_j = \{\sigma_1, \sigma_2, \ldots, \sigma_j\}$, is a simplicial complex. We require this property so that every step of our incremental algorithm is well defined. It should be clear that $K_{v_i} = K_j$ for $j = j_{i+1} - 1$.

Algorithm 1 MATRIX REDUCTION

1: $R = \Delta$
2: **for** $j = 1$ to m **do**
3:   **while** there exists $j_0 < j$ with $low(j_0) = low(j)$ **do**
4:     add colum j_0 to column j
5:   **end while**
6: **end for**

The persistence algorithm is easiest to describe as a matrix reduction algorithm, with the input matrix being the ordered bound-

ary matrix of K.[10] Specifically, this is the $m \times m$ matrix Δ whose rows and columns correspond to the simplices in the mentioned linear ordering. Specifically, the j-th column records the boundary of σ_j, namely $\Delta_{i,j} = 1$, if σ_i is a face of σ_j and the dimension of σ_i is one less than that of σ_j, and $\Delta_{i,j} = 0$, otherwise. Symmetrically, the i-th row records the star of σ_i. The persistence algorithm transforms Δ into *reduced form*, in which every row contains the lowest non-zero entry of at most one column. Making sure that we do not permute rows, and we add columns strictly from left to right, the lowest non-zero entries in the reduced matrix correspond to the birth-death pairs of the density field — precisely the information we are after. To describe the transformation, we write $low(j) = i$ if i is the maximum row index of a non-zero entry in column j, and we set $low(j) = 0$ if the entire column is 0. Algorithm 1 presents the algorithm for such a reduction. Section 4.4 illustrates these concepts and steps through an example.

The search for the fastest algorithm to reduce an ordered boundary matrix is an interesting question of active research in the field of computational topology. Most known algorithms use row and column operations, like in Gaussian elimination, which takes time proportional to m^3 in the worst case. A fortunate but largely not understood phenomenon is the empirical observation that some of these algorithms are significantly faster than cubic time for most practical input data. This is lucky but also necessary since we could otherwise not compute the results we present in this paper. The time to compute the persistence pairs for different models is displayed in Column 5 of Table 1.

4.3.1 Persistence Diagrams

Given the reduced boundary matrix, we generate the birth-death pairs of ϱ from the lowest non-zero entries in the columns. Specifically, for every non-zero $i' = low(j')$, the addition of $\sigma_{i'}$ gives birth to a homology class that dies when we add $\sigma_{j'}$. If $\sigma_{i'}$ is in the upper star of u_i, and $\sigma_{j'}$ is in the upper star of u_j, then we get (v_i, v_j) as the corresponding birth-death pair. It is quite possible that $i = j$, namely if both simplices belong to the same upper star, in which case we talk of a *still-birth*. We draw this birth-death pair as the point (v_i, v_j) in the *birth-death* plane. Alternatively, we can also draw them as $(v_i + v_j, v_j - v_i)$ in the plane. This amounts to a scaling by a factor of $\sqrt{2}$ and a rotation of coordinates by 45 degrees clock-wise. This is our preferred representation of the persistence diagrams throughout this paper. An illustration of the transformation is depicted in Figure 8. Drawing all points representing p-dimensional homology classes gives the *p-th persistence diagram* of f, which we denote as $\mathrm{Dgm}_p(f)$. Recall that the second coordinate is the persistence, and because a still-birth has zero persistence, it is drawn right on the horizontal axis. The persistence is a measure of significance of the feature represented by a birth-death point, and still-births are artifacts of the representation of f and have indeed no significance. The first coordinate is the sum of birth- and death-values, and we refer to half that coordinate as the *mean age*. It gives information about the range of density values the corresponding feature is visible.[11]

---

[10] We hasten to mention that storing this matrix explicitly is too costly for our purposes. Instead, we use the tessellation as a sparse matrix representation, and we implement all steps of the matrix reduction algorithm accordingly. However, for the purpose of explaining the algorithm, we maintain the illusion of an explicit representation of the matrix.

[11] Almost every homology class that is ever born will also die at finite time, but there are eight exceptions, namely the classes that describe the 3-torus
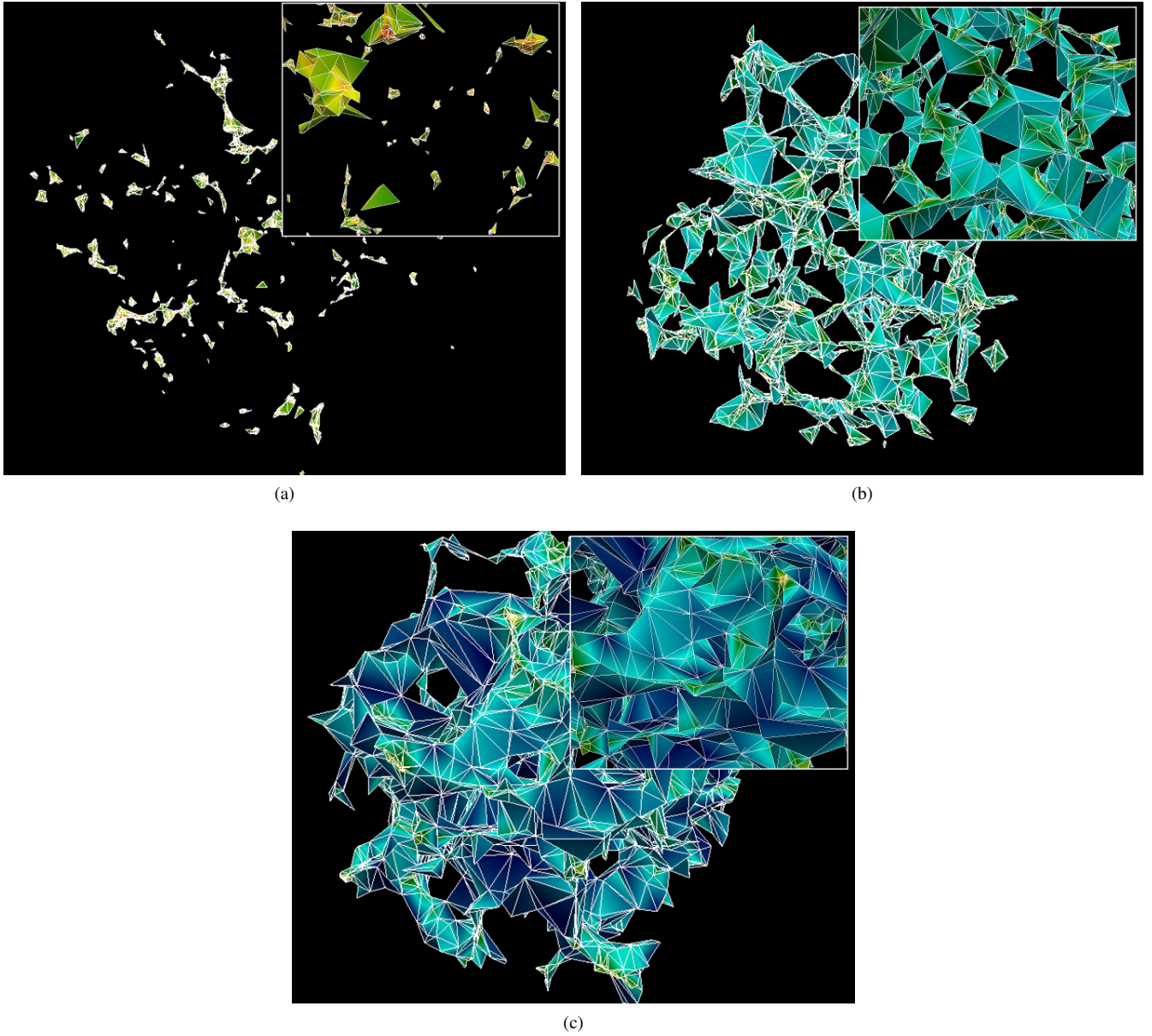
Figure 7. From panel (a) to panel (c): Growing superlevel sets of a filtration of a simplicial complex constructed on a discrete pointset. The insets present a zoomin. The density threshold decreases from left to right. As the density threshold decreases, more and more simplices from the underlying triangulation get included in the simplicial complex defined by the superlevel set corresponding to the density threshold.

Persistence diagrams contain more information than the Betti numbers. Indeed, we can read the p-th Betti number of the super-level set for ν as a number of points of $\mathrm{Dgm}_p(f)$. The contribution to the Betti numbers for the superlevel set at ν comes from all the dots in the persistence diagram corresponding to cycles that are born before ν and die after ν — in other words, the shaded region in panel (a) anchored at (ν, ν) in Figure 8. The shaded region transforms appropriately in panel (b) to a V-shaped region anchored at $(\nu, 0)$ on the horizontal axis. The arms of the V have slope -1 and 1 respectively. Another useful property is the stability of the diagram under small perturbations of the input. Specifically, the diagram

itself. They are not relevant for the study in this paper, and we do not draw them in the diagrams.

of a density function, f', that differs from f by at most ε at every point of the space, has bottleneck distance at most ε from $\mathrm{Dgm}_p(f)$; see (Cohen-Steiner et al. 2007). This implies that every point of $\mathrm{Dgm}_p(f')$ is at a distance at most ε from a point in $\mathrm{Dgm}_p(f)$ or from the horizontal axis.

4.3.2 Intensity Map

Our preferred visual presentation of a diagram is averaged over a number of realizations of the same random experiment; see Figure 13, which shows the plots for the data generated as described in Section 5. To construct it, we superimpose the diagrams of the different realizations, we discretize $\mathbb{R}^2$ using a grid of 100×100 squares, and we form the histogram by counting the points in each
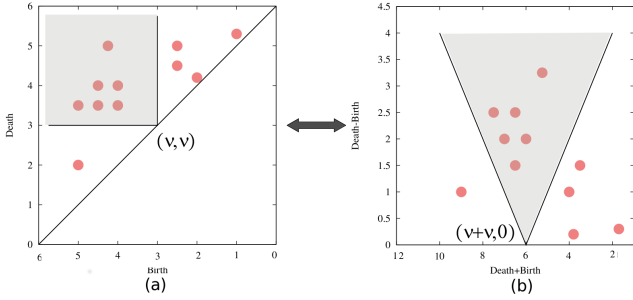
Figure 8. Figure illustrating the transition from the *birth-death* to the *mean age-persistence* plane. If the coordinates of a point in panel (a) are (b, d), the coordinates in panel (b) are $(d + b, d - b)$. The Betti numbers can be read off from the persistence diagrams. The contribution to the Betti numbers for a level set ν comes from all the persistent dots that are born before ν and die after ν — in other words, the shaded region in panel (a) anchored at (ν, ν). The shaded region transforms in panel (b) to a V-shaped region anchored at $(\nu + \nu, 0)$. The arms of the V have slope -1 and 1 respectively.

square. The result is a real-valued function on the plane, which we denote as the *averaged persistence diagram* or the *intensity map* of the diagram.

4.4 Example: Persistent Homology of a Triangle

In this section, we illustrate the construction of filtration and boundary matrix, and the subsequent reduction of the boundary matrix through an example. We take a triangle as our input simplicial complex.

4.4.1 Filtration

We assume there is a function defined on the simplices that constitute the triangle. The function is such that it induces an ordering of the simplices, from the lowest to the highest dimension. Figure 9 depicts such an ordering and the order in which the simplices appear in the filtration. We examine the filtration now, while simultaneously keeping track of the birth and death events.

First the vertex $\langle 1 \rangle$, appears in the filtration. this corresponds to the birth of a 0-dimensional hole, or an isolated object. Subsequently, vertices $\langle 2 \rangle$ and $\langle 3 \rangle$ appear, in that order, taking the number of isolated objects to 3. Thereafter, the edge $\langle 4 \rangle$ appears, merging the vertices $\langle 1 \rangle$ and $\langle 2 \rangle$ into a single component. We have a death of a 0-dimensional hole here. According to *elder rule* (Edelsbrunner & Harer 2010, page 150,), the component that forms early lives, and the younger component dies. In other words: the edge $\langle 4 \rangle$ kills the vertex $\langle 2 \rangle$, and $\{\langle 2 \rangle, \langle 4 \rangle\}$ form a birth-death persistence pair in the corresponding to a 0-dimensional hole. Thereafter comes edge $\langle 5 \rangle$, merging the vertex $\langle 3 \rangle$ with the connected component $\langle 1 \rangle$ (note that, since $\langle 2 \rangle$ is dead, the connected component resulting from the merger of $\langle 1 \rangle$ and $\langle 2 \rangle$ has the same index as $\langle 1 \rangle$).

The first topological hole in 1-dimension is born when the edge $\langle 6 \rangle$ appears in the filtration. This completes the boundary of the triangle, forming a loop. This 1-dimensional hole dies when the triangle appears in the final phase of the filtration, patching up the loop that had formed due to the introduction of the edge $\langle 6 \rangle$. In other words, $\{\langle 6 \rangle, \langle 7 \rangle\}$ form a birth-death persistence pair in 1-dimension.

In summary, there are three birth-death pairs in the filtration

of the triangle : two corresponding to isolated components — $\{\langle 2 \rangle, \langle 4 \rangle\}$ & $\{\langle 3 \rangle, \langle 5 \rangle\}$, and one corresponding to the loop — $\{\langle 6 \rangle, \langle 7 \rangle\}$.

From the point of view of need to construct the boundary matrix, we also enumerate the simplices and their boundaries here. The boundary of the edges constitutes of the vertices — for example, the boundary of the edge $\langle 4 \rangle$ consists of the vertices $\langle 1 \rangle$ and $\langle 2 \rangle$. The boundary of the trianguar face $\langle 7 \rangle$ consists of the edges $\langle 4 \rangle$, $\langle 5 \rangle$ and $\langle 6 \rangle$.

4.4.2 Boundary Matrix and its Reduction

We construct the boundary matrix, ∂ of the filtration of the triangle. Since the number of simplices in the filtration is 7 (three vertices, three edges, and one triangle), the size of the boundary matrix is 7×7. If the simplex i is in the boundary of the simplex j, the (i, j)-th element of the matrix is 1. All other elements are 0. We reduce the boundary matrix to R, using Algorithm 1, to the form detailed in Section 4.3. Figure 10 illustrates this operation in the form of the matrix multiplication notation $R = \partial \cdot V$, where R and ∂ are the reduced matrix and the original boundary matrix respectively. One may verify that the shaded entries in the ∂ matrix of Figure 10 indeed correspond to the simplices of the triangle, and its boundary (Figure 9 and Section 4.4.1).

4.4.3 Persistence Diagrams

It is easy to read off the persistence diagrams from the reduced matrix R. In Figure 10, the matrix R is the reduced matrix corresponding to the persistence homology computation of the filtration of a triangle. The shaded entries in this matrix have a value 1. Moreover, the entries in a deeper shade of pink denote the lowest row of a column whose entry is 1. The lowest 1's indicate the birth-death persistence pair. In this example, the lowest 1 entry indices correspond to the pairs $(i, j) \in \{(2, 4), (3, 5), (6, 7)\}$. The first entry in the pair is the index of the simplex that gives birth to a topolgcal hole. The second entry is the index of the simplex that kills that particular topological hole. One can verify that the indices of these pairs indeed correspond to the birth-death pairs, as enumerated in Section 4.4.1. Figure 11 presents the information of birth-death pairs in the filtration of a triangle in the form of persistence diagrams.

4.5 Points of Caution

The methods employed in this paper are perhaps on the more sophisticated end of the spectrum of cosmic web analyzes. It is therefore important to make sure that each step is rational and reliable, and the results are not contaminated by side-effects. There are indeed a few subtleties we need to keep in mind, and we list them here to avoid possible pit-falls.

- PERIODIC TILING. Instead of the 3-dimensional Euclidean space as a model of the Universe, we use the 3-torus, which has non-trivial homology, with Betti numbers $\beta_0 = 1$, $\beta_1 = 3$, $\beta_2 = 3$, and $\beta_3 = 1$. These numbers interfere with our statistical analysis of the topology of superlevel sets, but they are barely noticeable in the midst of usually thousands for ranks we observe.
- DENSITY FIELD ESTIMATION. Among the many possible density field estimators, we rely mostly on the DTFE as it naturally adapts to the particle distribution. It has the side-effect of forming high density spikes above particles that are completely and tightly surrounded by others.
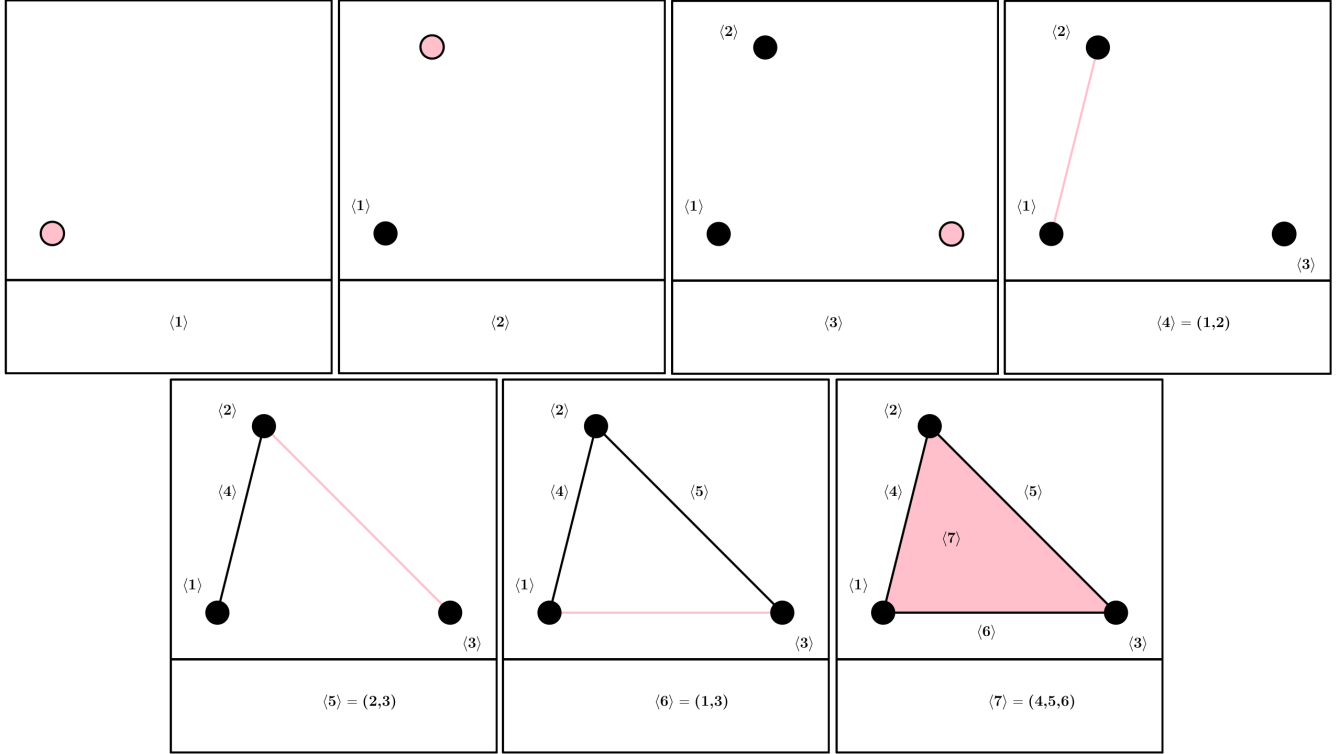
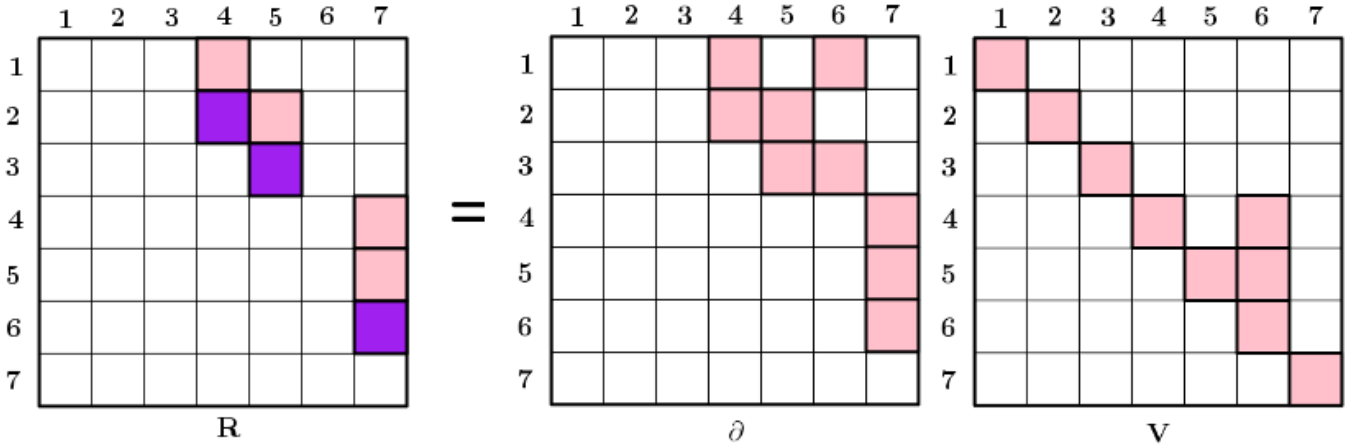**Figure 9.** Figure illustrating the order in which the simplices of the triangle appear in the filtration.

Figure 10. Figure illustrating reduction of the boundary matrix. R is the reduced matrix, ∂ is the original boundary matrix and V is the matrix whose column j encodes the columns of ∂ that add up to give the column j of R. The shaded entries in the matrices denote 1. All other entries are zero.

- SYMBOLIC PERTURBATION AND SUPERLEVEL SETS. We use the technical tools of symbolically perturbing the density values at the vertices, and retracting each superlevel set to the subcomplex above the threshold. Both techniques simplify the computation but have otherwise no effect. In particular, they give precisely the same persistence diagrams and intensity plots.
- INTENSITY MAPS. The averaged diagrams are meant to approximate the underlying distribution from which the persistence diagrams are sampled. We have no proof that they exist, other than the visual evidence that the diagrams for statistically similar particle distribu-

tions appear similar. We draw these plots by counting points within each square of a 100×100 grid, which implies that small shifts of the grid would give (slightly) different plots.

- PERTURBATIONS AND STABILITY. Recalling the Stability Theorem for persistence diagrams (Cohen-Steiner et al. 2007), we note an ε-perturbation of the density function can lead to the addition or removal of points at distance at most ε from the horizontal axis. As a consequence, the intensity plots may change an arbitrary amount near the horizontal axis, but not at a distance larger than ε.
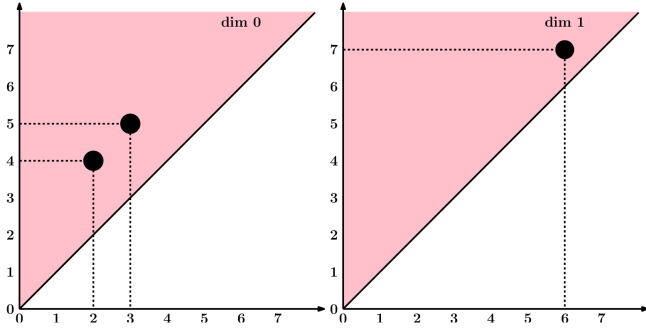
Figure 11. Persistence diagrams corresponding to the birth-death pairs in the filtration of a triangle. Left panel presents the 0-dimensional persistence diagram, corresponding to birth-death or merger events of isolated objects. Right panel presents the 1-dimensional persistence diagram, corresponding to birth-death events of loops.

5 RANDOM TOPOLOGY

Random processes play a crucial role in many aspects of life. In this paper, the analysis of random data provides a baseline for comparison, training the eye to pay attention to features that are not accidental, caused by inevitable random configurations in the data. We create this baseline by picking particles in space uniformly at random.

5.1 Poisson Point Process

Recall that our model of the Universe is the 3-dimensional cube with opposite faces glued to each other to create a periodic tiling of space. We call this the 3-*torus model*, denoting it by $\mathbb{M}$. We choose the length unit such that each edge is $200h^{-1}$Mpc long. Within this cube, we pick $n = 500,000$ particles in a *Poisson point process*[12]. For practical purposes, the particles are thus chosen from a *uniform distribution* over the 3-torus. This forms a reasonable approximation of a Poisson point process.

5.2 Graphs of Betti Numbers

To get a feeling for the DTF estimator of the particle sample, we compute the Betti numbers of the superlevel sets. Writing $f : \mathbb{M} \to \mathbb{R}$ for the estimated density function, we plot the p-the Betti number of $f^{-1}[\nu, \infty)$ as a function of ν, for $p = 0, 1, 2$. Drawing ν decreasing from left to right, we superimpose the graphs of the Betti numbers for ease of comparison; see Figure 12. We observe that the graph of β_0 peaks first, at a density threshold of $\nu \approx 0.04$. As expected, the graph of β_1 peaks second, at $\nu \approx 0.015$, and the graph of β_3 peaks last, at $\nu \approx 0.007$. This suggests that loops are formed preferably by merging clusters into filaments, as opposed to growing horns that eventually meet. Similarly, voids are formed preferably by merging clusters and filaments into walls that eventually meet to completely enclose junks of empty space. In addition to the clear order, we observe that each of the three graphs has a clean shape with a clearly defined single mode. These properties are indicative of the data following a single, well-defined distribution.

5.3 Averaged Persistence Diagrams

As explained in Section 3, persistence diagrams contain strictly more information than the graphs of the Betti numbers. Figure 13 shows the intensity maps of the density function, $f : \mathbb{M} \to \mathbb{R}$, again in log-log scale. To compare these plots with the curves in Figure 12 on the right, we observe that the number of birth-death pairs, (ν_b, ν_d), with $\nu_b \geqslant \nu > \nu_d$ gives the Betti numbers for the super-level set for threshold ν.[13] Since we draw the diagrams as intensity maps, we need to compare the integral over the V-shaped region anchored at the point $(\log \nu + \log \nu, 0)$ with the Betti number at $\log \nu$. When doing this, note that the horizontal axes in Figure 12 are labeled with values of ν, while the horizontal axes in Figure 13 are labeled with twice the logarithm to the base 10 of ν. Similar to the graphs in Figure 12, the diagrams of $\beta_0, \beta_1, \beta_2$ are ordered along the horizontal axis. In addition, the persistence, which we see as the vertical distance from the horizontal axis, decreases from β_0 to β_1, and then again from β_1 to β_2. This is a reflection of the DTF estimator, which tends to form spikes of high density at clusters. The height of these spikes is measured by the persistence of dots in the diagram of β_0, and these spikes are visible even after taking the logarithm of the density. In contrast, the depth of voids is measured by the persistence of the dots in the diagram of β_2, which is much milder, as seen in Figure 13. Finally, we point out the characteristic "pointed hat" shape of the diagrams, and more specifically the sideways leaning tips for β_0 and β_2. These shapes seem related to heavily studied but difficult questions in percolation theory, and in particular to threshold phenomena, which are characteristic of this field.

5.4 Scaling Relations of Poisson Topology

In order to probe the scaling relations of various quantities for the uniform distribution, we constuct realizations with different mean inter-particle separation $\lambda = 0.0625, 0.125$, and 0.25. Keeping the box size same, this amounts to an increased number of particles with decreasing λ. Figure 14 plots the Betti numbers for realizations with different λ, where the horizontal axis (density threshold) is scaled with the variance of density. The β_is for different λ's have the same peak positions after scaling. Peak positions are well separated, denoting that topology is predominantly either "meatball-like", "sponge-like" or "cheese-like" at different values of ν. β_0 peaks at $\nu \approx 1.8$, β_1 at $\nu \approx 0.6$ and β_2 at $\nu \approx 0.3$. The coincidence of peak-positions suggest a functional form of Betti numbers as a function of density threshold.

In addition to the scaling of peak positions with normalized density threshold values, the peak amplitudes and the location of the peak of the β_i also scale with λ. This scaling is shown in the top-left and top-right panels of Figure 15. Peak amplitudes of β_0, β_1 and β_2 scale linearly with λ, with different slopes. β_1, the number of loops rises the sharpest with λ, with a slope of $m = 0.08902$, followed by β_0 ($m = 0.05036$) and β_2 ($m = 0.00989$). The non-normalized (with respect to variance) peak positions on the horizontal axis also scale with λ. However, the trend is not the same as the peak amplitudes. In this domain, ν_0, the peak position for β_0 rises the sharpest with increasign λ, with a slope of $m = 0.57749$, followed by ν_1 ($m = 0.2299$) and ν_2 ($m = 0.11004$), in that order. The number of simplices per unit volume also scales linearly with

---

[12] The Poisson process depends on a density parameter that determines the expected number of particles. We slightly rig the process such that the number of chosen particles is precisely the expected number.

[13] This relation may be violated by the $8 = 1 + 3 + 3 + 1$ essential homology classes of the 3-torus, which are not drawn in our diagrams. Their number is too small to be notices in our figures.
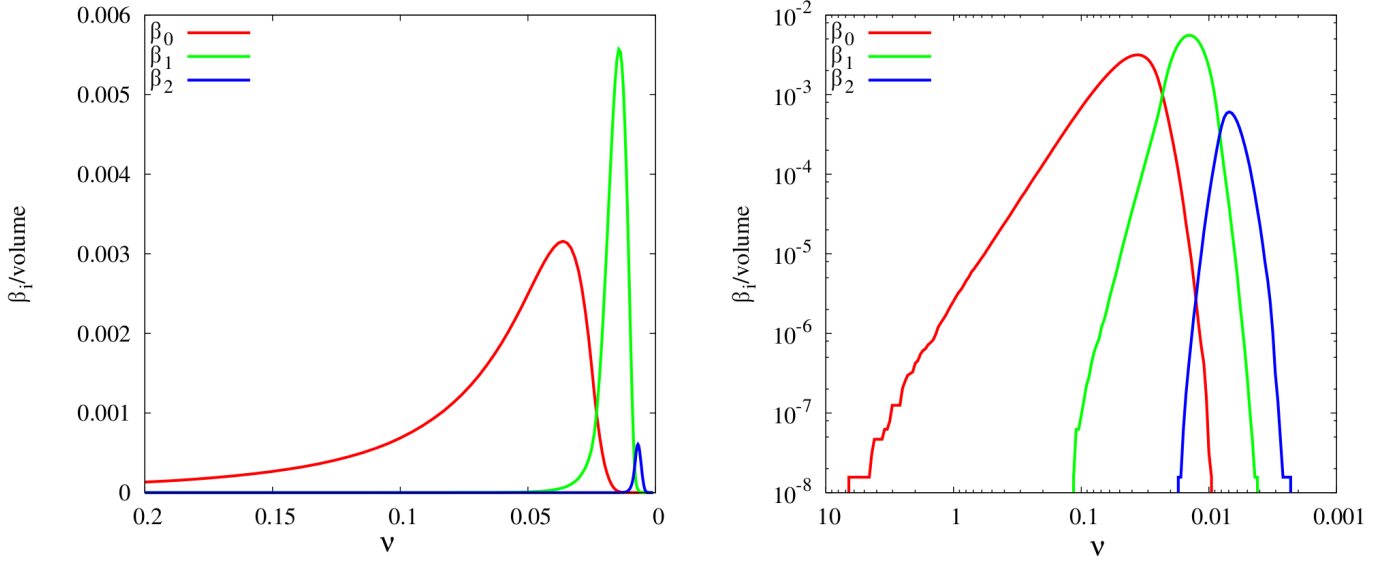
Figure 12. Left: The three Betti numbers of the superlevel sets of a density function on the 3-torus. The threshold, ν, decreases from left to right, and the numbers of components, tunnels, and voids increase from bottom to top. Generating $500{,}000$ particles in a Poisson process, we get the density with the DTF estimator as explained in Section 2. The graphs are averaged over ten realizations. Right: the same graphs in log-log scale.
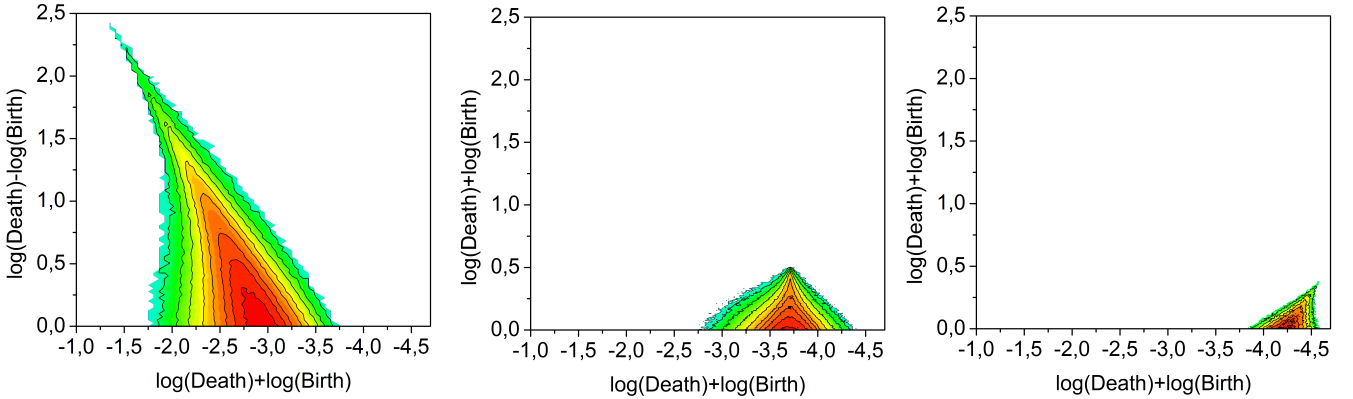

Figure 13. From left to right: the intensity maps of the persistence diagrams for dimensions $0, 1, 2$, averaged over ten realizations. The sum of the logarithms of birth- plus death-values decreases from left to right, while the logarithm of the persistence increases from bottom to top.

λ and has a slope of $m = 29.07$. This is presented in the bottom-left panel of Figure 15. The bottom-right panel of Figure 15 presents the scaling of time required to compute persistence for the uniform distribution with respect to the number of simplices in the tessellation. The time required to compute persistence seems to follw a power-law with respect to the number of simplices. We fit a power-law of the form $f(x) = ax^b$ where b is the index of the power-law. The fitted curve to the data points gives the value of the index $b = 2$.

6   SINGLE-SCALE TOPOLOGY

In this section, we consider a random process that produces particle distributions near the elements of a fixed Voronoi tessellation. While heuristic in nature, these distributions mimic the structural patterns observed in the Universe: the clusters, filaments, and walls in the Cosmic Web.

In these Voronoi clustering models, a geometrically fixed Voronoi tessellation defined by a small set of nuclei is complemented with a heuristic prescription for the location of particles

or model galaxies within the tessellation (van de Weygaert & Icke 1989; van de Weygaert 1991; van de Weygaert 2007). We distinguish two classes of Voronoi models: the *pure Voronoi element models* and the *Voronoi evolution models*. Both are obtained by moving an initially random distribution of N particles toward the faces, lines, and nodes of the Voronoi tessellation. The pure Voronoi element models do this by a heuristic and user-specified mixture of projections onto the various geometric components of the tessellation. The Voronoi evolution models accomplish this via a gradual motion of the galaxies from their initial, random locations towards the boundaries of the cells.

6.1   Pure Voronoi Element Models

Recall that a Voronoi tessellation in space has four types of elements: vertices, edges, faces, and cells. Constructing and fixing a diagram for only 32 nuclei within a periodic box with sides of length $200h^{-1}$Mpc, we consider three random processes that generate particles near the vertices, edges, and faces. With each realization, we get $262{,}144$ particles distributed uniformly along and with
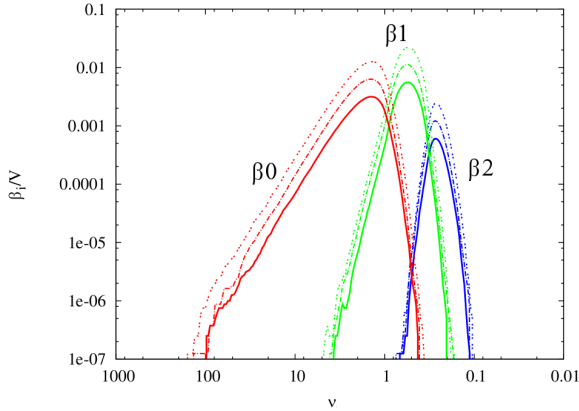
Figure 14. Betti numbers for the uniform distribution with λ, the parameter of distribution varying. For each realization, the levelset values on the horizontal axis are normalized by the standard deviation of that particular realization. In the representation of normalized horizontal axis, the peak positions for realizations with different λ are coincident. The lowest peak-amplitude corresponds to $\lambda = 0.25$, followed by $\lambda = 0.125$ and 0.0625 respectively.

a Gaussian spread of $1h^{-1}$Mpc around the elements of the Voronoi skeleton; see Figure 16. The first process generates the particles in *clusters* around the vertices, the second forms *filaments* along the edges, and the third creates *walls* following the faces. Since each process focuses on the elements of a single dimension, we call the resulting distributions *pure Voronoi element models*.

6.2 Graphs of Betti Numbers

We begin our analysis by looking at the Betti numbers of the superlevel sets of the estimated density field. Figure 17 shows the numbers as functions of the threshold. All results are averaged over eight realizations. The number of particles being the same in all three models, the average density in the clusters is higher than along the filaments, which in turn is higher than inside the walls. This is reflected by the graphs of β_0, in which the density threshold of the maximum is highest for clusters, between the extremes for filaments, and lowest for walls. The value at the maximum (the number of components) follows an opposite trend.

Note the prominent shoulder in the graph of β_0 for clusters, which we do not see in the graphs for filaments and voids. The shoulder is a reflection of the merging process, which first consolidates the particles into clusters and second merges the clusters into one connected whole. We thus observe a transition from *intra-cluster* to *inter-cluster* merging, with the parameters of the shoulder identifying the density values at which this transition happens. In the filament and wall models, we have a single connected component as soon as all filaments and walls have been consolidated, which explains the absence of shoulders. Nevertheless, we observe a transition from a focus on intra- to inter-structural connectivity as a function of the density threshold. Indeed, the graph for β_1 has a shoulder, both for clusters and for filaments, and the explanation is similar.

Continuing the trend, the graph for β_2 has two clear modes for clusters and filaments, and a hint of two modes for voids. A comparison with the intensity maps shows that this hint is a fluke, and while the separation into two populations of voids is real, it is not visible in the graph. More about this shortly. Returning to the

graphs of β_2, we note that the left modes reflect the consolidation of the particles sampling the Voronoi elements, and the second modes reflect the filling up of the global, inter-structural voids. We see that the ordering of the left modes from clusters to filaments to walls is reversed for the right modes, remembering that β_2 for walls does not distinguish between the two populations and combines the left and right modes into one. The reversal of order makes geometric sense, since we are talking about the same voids in all three models, but these voids are shallower and appear at lower density values for clusters than for filaments, and more so for walls.

6.3 Averaged Persistence Diagrams

The intensity maps for the pure Voronoi element models display features the graphs of the Betti numbers fail to capture, primarily because the maps distinguish between significant and insignificant features. For example, each realization of the filament model has a large number of tiny loops inside the filaments, but also a smaller number of larger loops that are carried by the filaments themselves. The 1-st averaged persistence diagram distinguishes between these two populations.

More generally, Figure 18 shows the intensity maps of all diagrams for all pure Voronoi element models: from top to bottom for clusters, filaments, voids, and from left to right for β_0, β_1, β_2. To a first degree of approximation, all diagrams contain a red and green high-intensity region and a blue low-intensity region. For the six diagrams in the upper-right triangle of the 3×3 array, the second region forms a *island*, by which we mean a hill that is completely surrounded by a ring of zero intensity. As before, the high-intensity regions reflect the intra-structural consolidation, while the low-intensity regions consist of points that represent large topological structures each carried by several clusters, filaments, or walls. For components, the two populations are clearly separated in the upper-left diagram for clusters.

Similar to the graphs, we see no separation into the two populations of components in the diagrams for filaments and walls. For loops, the two populations are most clearly separated in the center diagram of Figure 18, which plots the intensity for filaments. The two populations of loops are less clearly separated in the top diagram for clusters, and not at all separated in the bottom diagram for walls. Nevertheless, that map has a tongue suggesting a population of loops emigrating from the bulk. The geometric interpretation of this phenomenon is that the walls meet in filaments, which are therefore more densely sampled, so that global loops can form before the walls are completely filled.

For voids, the separation into two populations is clearly visible in all three diagrams; see the third column in Figure 18. Most noteworthy is the separation in the bottom diagram, in which the two populations have roughly the same mean age but very different persistence. Such populations cannot be separated by V-shapes, which is the reason the function of Betti numbers is oblivious to this difference.

7 MULTI-SCALE TOPOLOGY

One of the major features of the matter distribution at large scales is the presence of a hierarchy of substructures, with a large dynamic range in density and spatial scale. As a result, we see a multi-scale distribution, with interesting features at every scale.
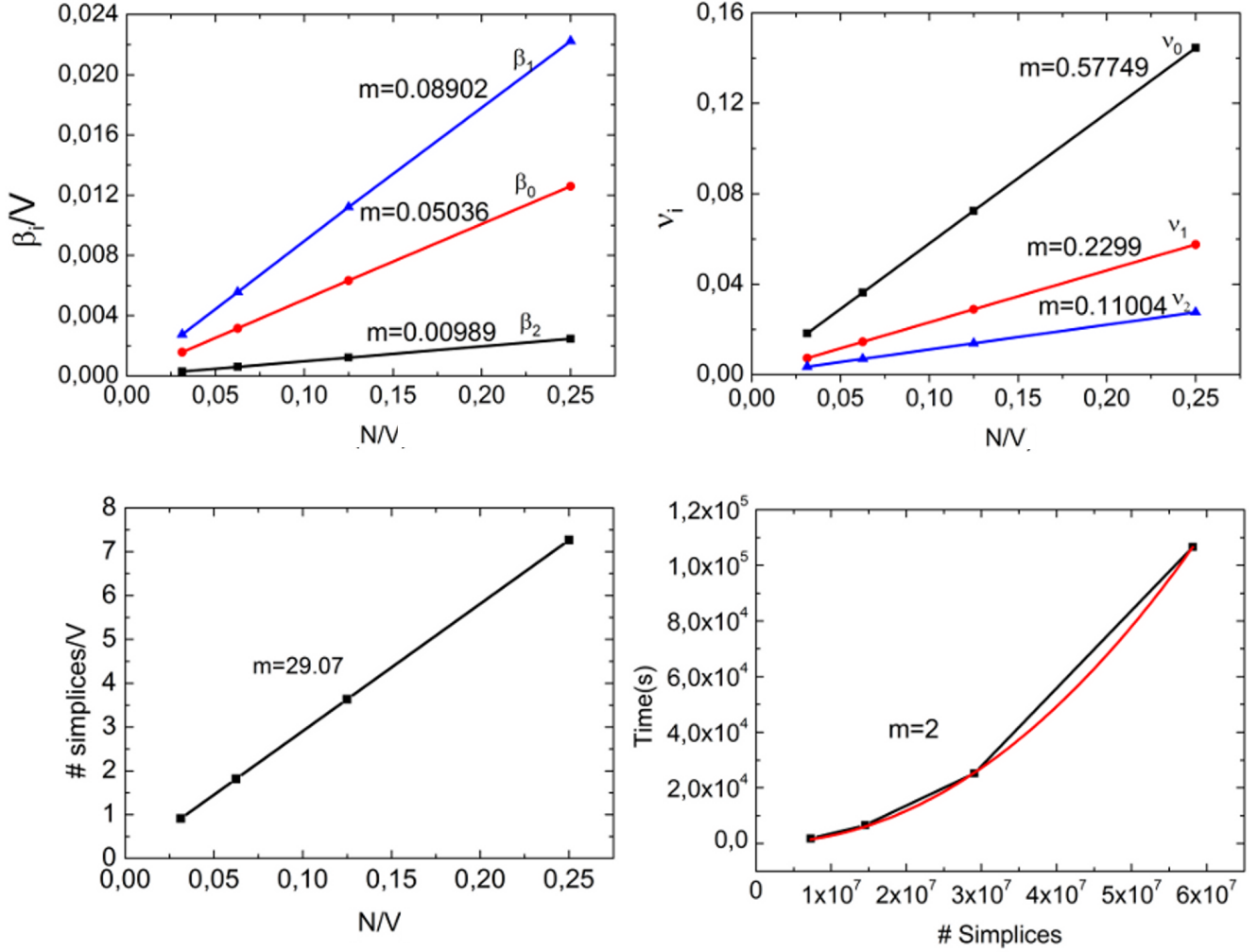
Figure 15. Scaling relations for different quantities for the uniform distribution. The quantities on the vertical axis (except the bottom-right panel) are per-unit-volume. Top-left panel : Scaling of peak-amplitude of β_0, β_1 and β_2, with number of particles per unit volume. Top-right: scaling of un-normalized (with the standard deviation) peak-position (on the horizontal axis), with the mean number of particles per unit volume. Bottom-left: scaling of number of simplices with λ. This can be translated to the scaling of number of simplices with the number of particles in the box. Bottom-right : scaling of time required to compute persistence with the number of simplices. The quantities on vertical axis scale linearly with quantities on horizontal axis in the top-left, top-right and bottom-left panel. The scaling in bottom-right panel has a power-law form. the slope of scaing is denoted by "m" in the first three panels. In the fourth panel, m is the index of the power-law distribution.

7.1 The Soneira–Peebles Model

Soneira–Peebles is a random point process with adjustable parameters that generates a fractal distribution of particles (Soneira & Peebles 1978). Both the two-point correlation function and the fractal dimension of these particle sets are well understood analytically. The parameters can be chosen such that the correlation function of the particle distribution mimics that of the galaxies in the sky. It is used to explain the clustering statistics of the galaxy distribution, taking into account the fact that they display strong self-similarity. The placement of the particles is controlled by three parameters, each responsible for tuning a different aspect of the hierarchy:

η: the *height*, equal to the number of levels minus 1;
ζ: the *concentration*, equal to the ratio between consecutive radii;
ψ: the *branching factor*, equal to the number of children.

We start the construction with a unit sphere at level 0, inside

which we place the centers of ψ level-1 spheres, each with radius $1/\zeta$ at random positions. The next iteration places the centers of ψ level-2 spheres with radius $1/\zeta^2$ inside each level-1 sphere. We continue the process until we reach level η, with a total of ψ^η spheres of radius $1/\zeta^\eta$. Finally, we pick a particle at the center of each level-η sphere. Figure 19 shows three sample distributions with fixed height and branching factor, but with varying concentration.

While this produces a pure *singular* Soneira–Peebles model, it is common to superimpose a number of them to produce a somewhat more realistically looking model of the galaxy distribution.

The Soneira–Peebles model involves a hierarchy of structures of varying densities and characteristic scales, with the higher level spheres corresponding to high density structures of small scale and the lower level spheres corresponding to low density structures of large scale. As each sphere is constructed in the same way, the resulting point distribution is self-similar, forming a bounded fractal.
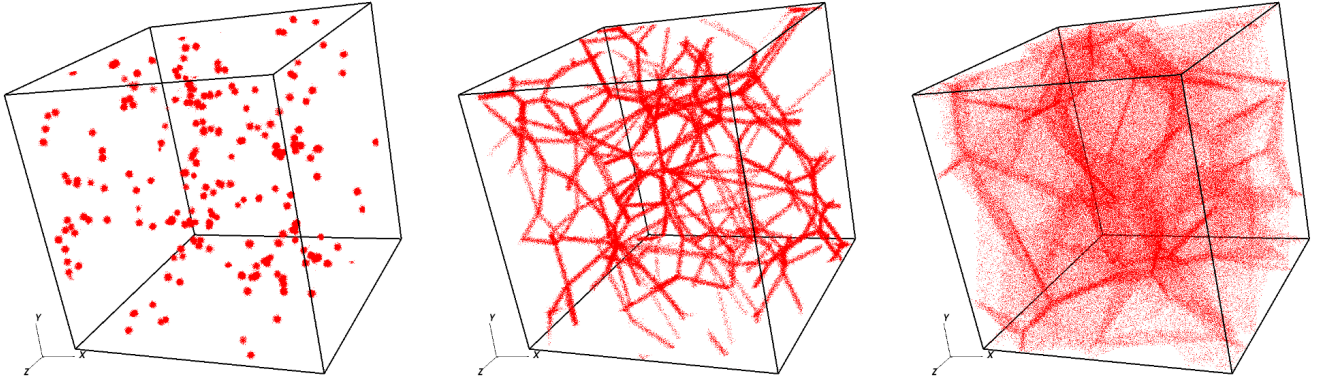
Figure 16. Top row, from left to right: particle distribution in the three pure Voronoi element models corresponding to clusters, filaments, and walls. Each data set consists of 262, 144 particles inside a periodic box of side length $200h^{-1}$Mpc. Bottom row, from left to right : density rendering of the same.
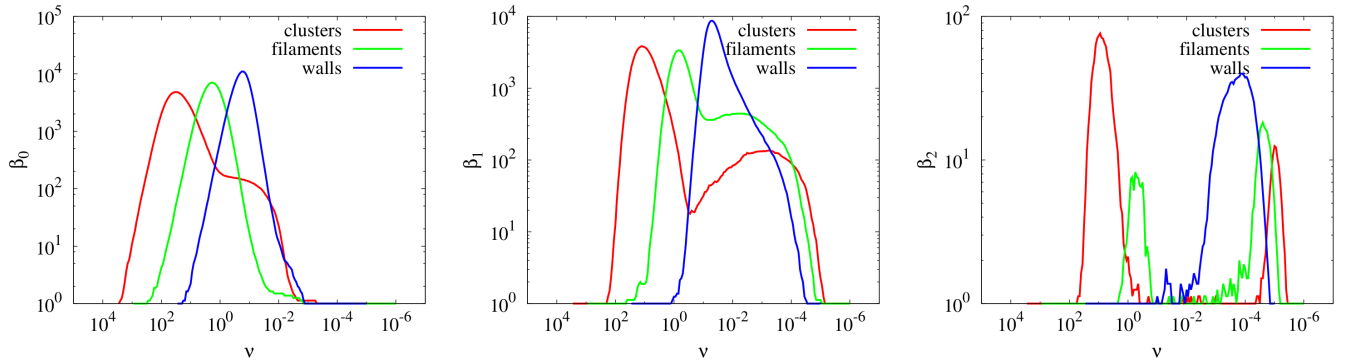

Figure 17. The Betti numbers of the superlevel sets of the density function for pure Voronoi element models as functions of the threshold. From left to right: $\beta_0 \beta_1, \beta_2$.

The fractal geometry of a point set is often characterized by the fractal dimension, D, which is defined as

$$D = \frac{\log N(r)}{\log(1/r)}, \qquad (23)$$

in which $N(r)$ is the number of non-empty cells in a partition of constant cell size r. If the Soneira–Peebles model would contain an infinite number of levels, the resulting point distribution would have fractal dimensions $D = \log \psi / \log \zeta$. One important manifestation of the self-similarity is reflected in the power-law two-point correlation function. For 3 dimensions, it is given by $r^{-\gamma}$, with

$$\gamma = 3 - \frac{\log \psi}{\log \zeta}, \qquad (24)$$

for $1/\zeta^{\eta-1} < r < 1$. The parameters ψ and ζ may be adjusted such that they yield the desired value for the correlation slope, γ.

7.2 Graphs of Betti Numbers

We study particle distributions generated with height $\eta = 6$, branching factor $\psi = 9$, and three different concentrations, $\zeta = 5.0, 7.0, 9.0$. For each parameter triplet, we average the results over eight realizations. Figure 20 shows the Betti numbers as functions of the threshold defining the superlevel set of the density functions

defined by the particle distributions. Evidence of modularity[14] is present in the curves for all chosen values of ζ. For β_0, it manifests itself as ripples on the right side of the mode, when the number of components decreases after reaching a maximum. For β_1 and β_2, the evidence can be seen in the number of modes. Higher concentration results in a more clearly defined modular distribution. Indeed, the number of distinct ripples in the graphs for β_0 is the largest for $\zeta = 9.0$, while they are barely visible for $\zeta = 5.0$.

The peak amplitude for β_0 is the same for all three distributions. The reason may be trivial, namely the fact that η and ψ are the same for all three experiments, implying that all data sets contain the same number of particles, namely $\psi^\eta = 9^5$. However, the peaks occur at different density thresholds, reflecting the varying local density of the distributions generated for different concentrations. Indeed, more concentrated particle distributions have higher density peaks, and as a result we see the mode at higher thresholds. We observe the same trend in the curves for β_1, and even for β_2, although the latter curves a much rougher, reflecting overall smaller numbers and more noise. The number of levels in the hierarchy is reflected in the number of peaks in the graph of β_1. We see five distinct peaks, while the number of levels in the distribution is six. It seems that the lowest level has too few components to be visible in

---

[14] The term "modularity" is used for particle distributions with distinguishable levels in the hierarchy. A *modular* distribution is hierarchical in nature.
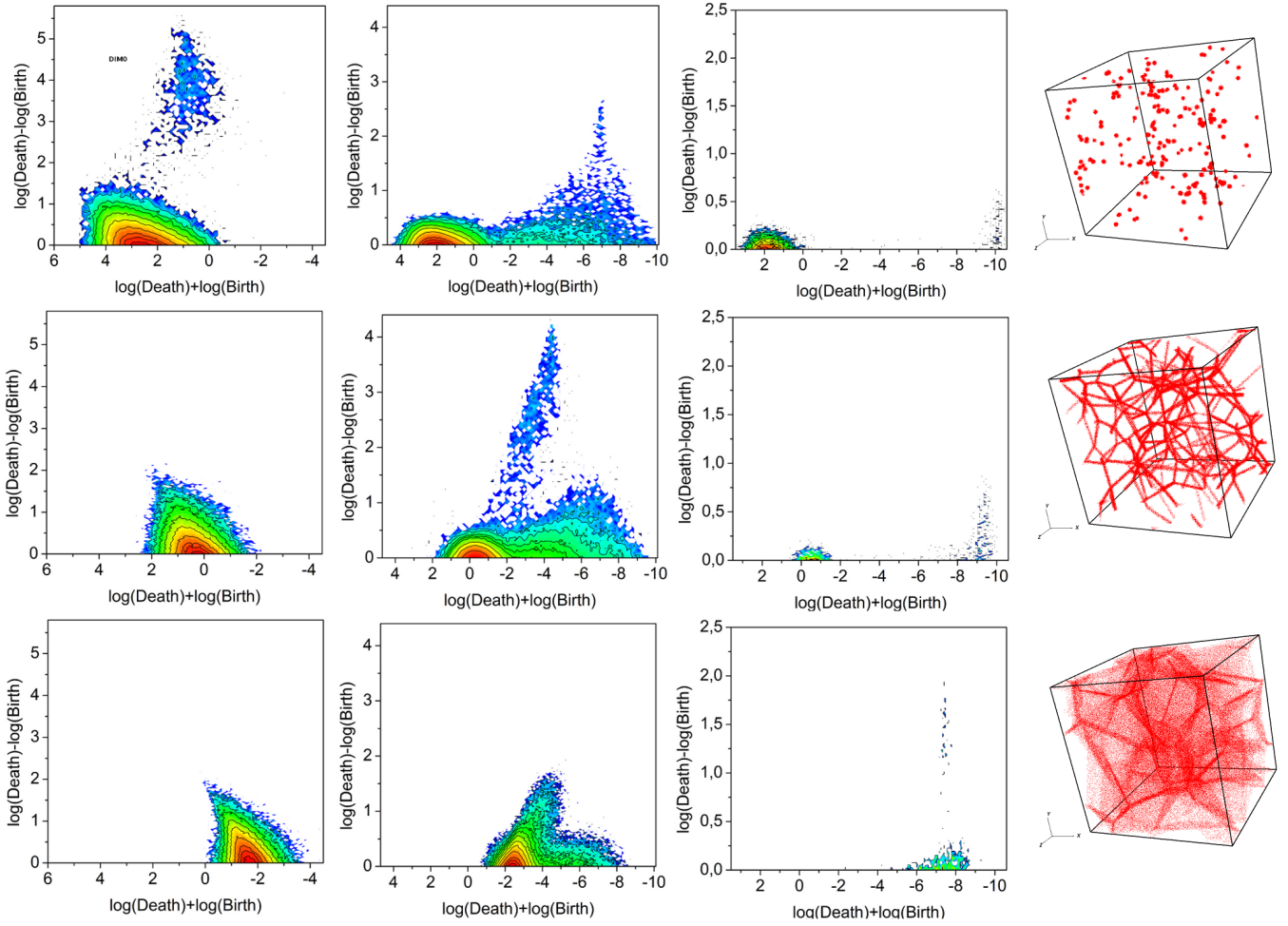
Figure 18. The averaged persistence diagrams of the density functions for pure Voronoi element models. From top to bottom, we show the intensity for clusters, filaments, walls, and from left to right for classes of dimension 0, 1, 2.

the graphs. While the graphs of β_2 are noisy, they also exhibit five distinct peaks.

7.3   Averaged Persistence Diagrams

The intensity maps of the particle distributions described above are shown in Figure 21, for $\zeta = 5.0, 7.0, 9.0$ from top to bottom, and for dimension 0, 1, 2 from left to right. The features in the diagrams show a clear transition as a function of the concentration, with evidence of modularity present in all diagrams. In particular, we notice *hills* in the intensity, which we define as the neighborhood of a local maximum away from the horizontal axis. Note that these are different from *tongues* in the intensity maps, which are local persistence maxima.

Hills seem rather unusual features as the intensity usually decreases monotonically from bottom to top. For the 0-dimensional diagrams, we notice an increase in the number of hills when we increase the concentration: there is a single hill for $\zeta = 5.0$, we see the hint of a second hill for $\zeta = 7.0$, and there are three clear hills for $\zeta = 9.0$. In words, we get progressively more evidence for modularity as the concentration increases, which is hardly surprising. Interestingly, the hills come in sequence, from bottom to top, so that later hills represent birth-death pairs of higher persistence. Furthermore, the intensity of the hills decreases from bottom

to top. This makes sense since lower levels in the construction contain fewer clusters with lower persistence. Indeed, the highest level in the hierarchy generates the densest regions with the largest number of particles. Physically this means that many tiny clusters form at high density thresholds. These clusters are short lived, and as we go down from the highest level, a large number of tiny clusters merge together to form fewer but larger clusters. These larger clusters are of higher persistence and correspond to the low-intensity, high-persistence hills in the diagrams. The bias of the higher persistence hills towards the lower density values, is interesting, as it counters the higher density leaning pointy hat shape we see for the uniformly distributed particles in Figure 13.

Progressively better defined modularity as a function of increased concentration is also evident in the 1-dimensional intensity maps. Here, we see tongues that correspond to the hills in the 0-dimensional maps. Larger concentration corresponds to smaller filling rate, which results in bigger patches of empty space. This is reflected in the 2-dimensional intensity maps, which record the information for the voids or empty regions: we see three or perhaps four grainy tongues, which are fuzzy for $\zeta = 5.0$, and progressively better defined for $\zeta = 7.0$ and 9.0.
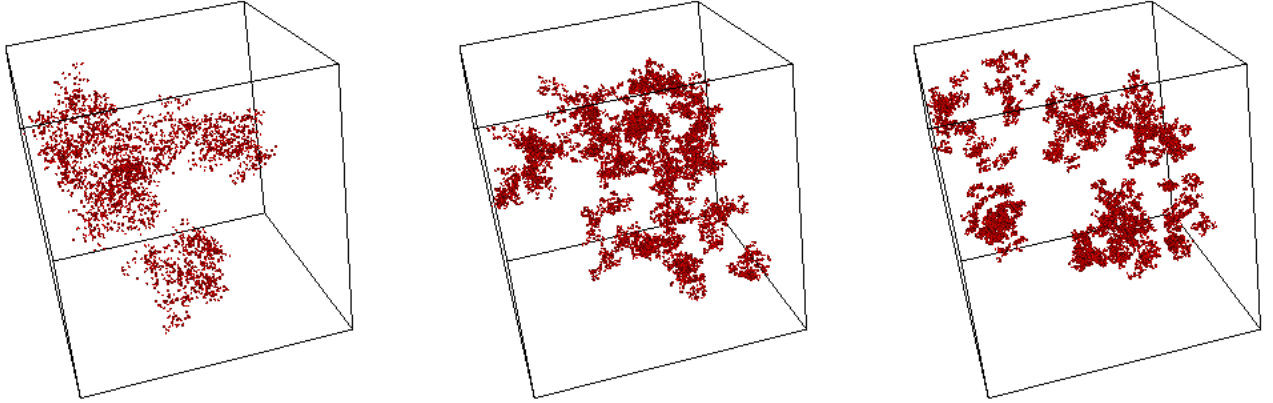
Figure 19. Particle distributions generated with the Soneira–Peebles process. Fixing the height to $\eta = 6$ and the branching factor to $\psi = 9$, we vary the concentration from left to right as $\zeta = 5.0, 7.0, 9.0$. There are 6^9 particles in each dataset. The apparent low number of particles to the naked eyes is due to the high concentration factor. Zooming into a particular region shows similar structure at higher levels of hierarchy. Density rendering of the distribution is not feasible due to high concentration.
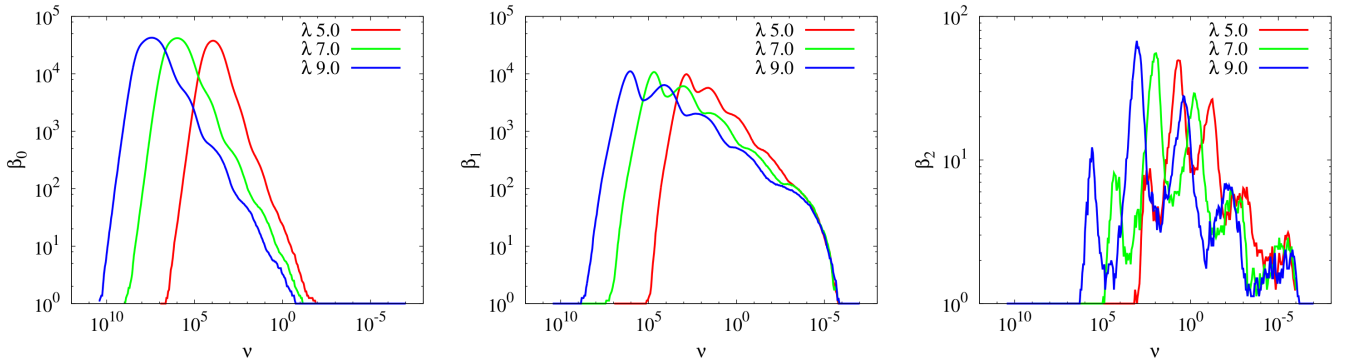
Figure 20. From left to right: the 0-th, 1-st, 2-nd Betti numbers of the superlevel sets of the density function for the Soneira–Peebles particle distributions plotted on a logarithmic scale. Fixing the height to $\eta = 5$ and the branching factor to $\psi = 9$, we vary the concentration as $\zeta = 5.0, 7.0, 9.0$.

8 DYNAMIC TOPOLOGY

In this section, we consider particle distributions that change over time, similar to the matter in the Cosmos. Under the influence of gravity, the relatively uniform distribution at early epochs accumulates in the potential wells, evolving into galaxies and clusters. These clusters seem connected by filaments and walls.

8.1 Voronoi Evolution Models

Starting with a random distribution of particles over the entire volume, *Voronoi evolution* generates a time-series of particle distributions driven by slow drifts from higher- to lower-dimensional elements of an underlying Voronoi tessellation. They attempt to provide weblike galaxy distributions that reflect the outcome of realistic cosmic structure formation scenarios. They are based upon the notion that voids play a key organizational role in the development of structure and makes the Universe resemble a soapsud of expanding bubbles (van de Weygaert & Icke 1989). While the galaxies move away from the void centres, and stream out of the voids towards the sheets, filaments and clusters in the Voronoi network the fraction of galaxies in the voids (cell interior), the sheets (cell walls), filaments (wall edges) and clusters (vertices) is contin-

uously changing and evolving. The details of the model realization depends on the time evolution specified by the particular Voronoi Evolution Model.

Within the class of Voronoi Evolution Models the most representative and most frequently used are the *Voronoi kinematic models*. They form the idealized and asymptotic description of the outcome of hierarchical gravitational structure formation process, with single-sized voids forming around depressions in the primordial density field. This is translated into a scheme for the displacement of initially randomly distributed galaxies within the Voronoi skeleton. Within a void, the mean distance between galaxies increases uniformly in the course of time. When a galaxy tries to enter an adjacent cell, the velocity component perpendicular to the cell wall disappears. Thereafter, the galaxy continues to move within the wall, until it tries to enter the next cell; it then loses its velocity component towards that cell, so that the galaxy continues along a filament. Finally, it comes to rest in a node, as soon as it tries to enter a fourth neighbouring void.

We have sampled the time-series at three moments in time, called *stages*, and we show the results for these, emphasizing the continuous change that becomes visible by comparing the graphs and diagrams. To parametrize the stages, we keep track of the percentage of particles that lie in the interior of cells, faces, edges, and
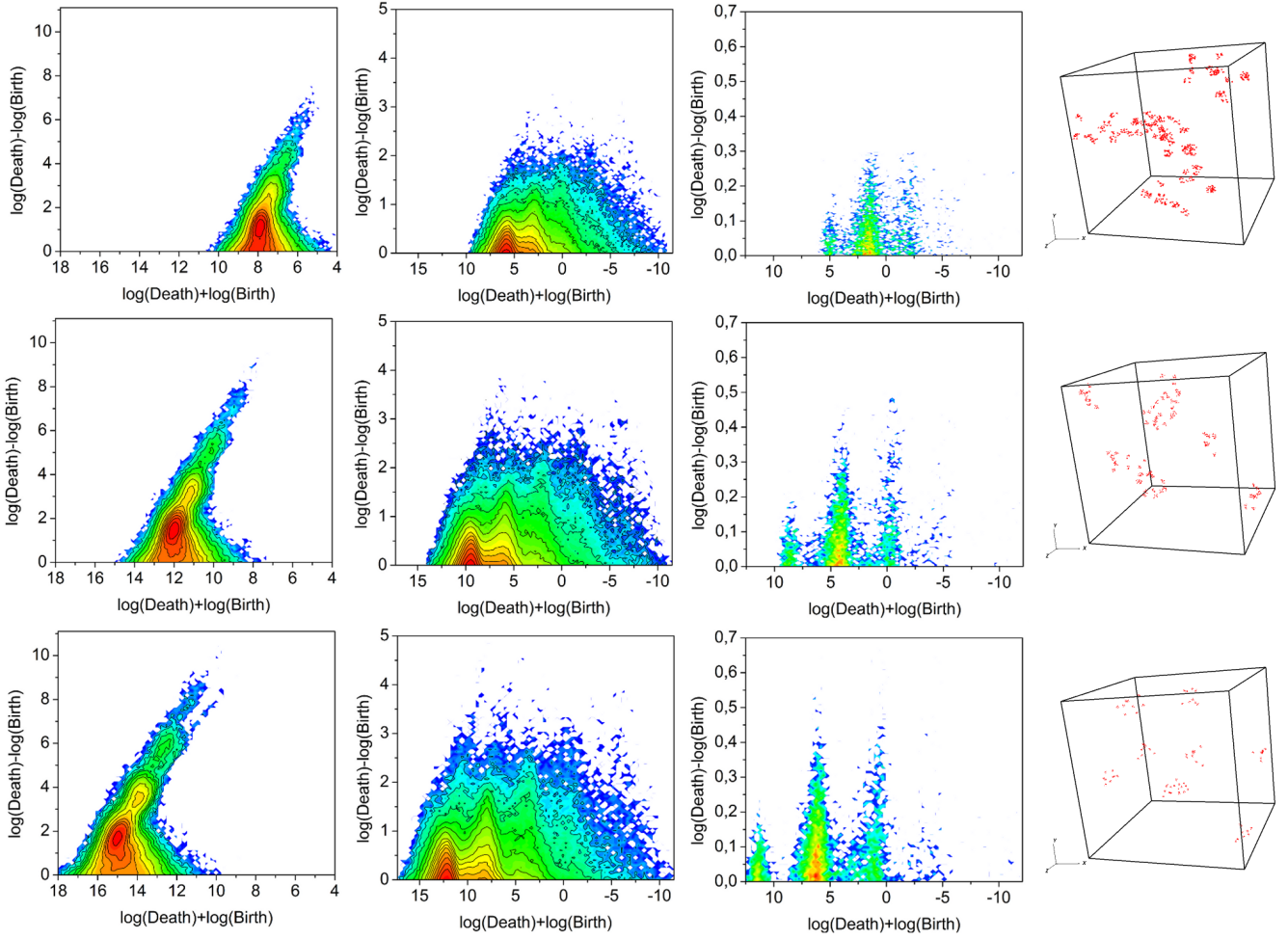
Figure 21. From left to right: the 0-, 1-, 2-dimensional averaged persistence diagrams of the density functions obtained from the Soneira–Peebles particle distributions. Fixing the height to $\eta = 5$ and the branching factor to $\psi = 9$, we vary the concentration from top to bottom as $\zeta = 5.0, 7.0, 9.0$.

	cell	wall	filament	cluster
Stage 1	49.93%	38.52%	10.46%	1.08%
Stage 2	5.03%	23.50%	41.26%	30.22%
Stage 3	2.00%	14.72%	39.81%	43.47%

Table 2. The relative abundance of particles in each structural element throughout the course of evolution. Stage 1 is the least evolved, with almost half the particles residing in cells, while Stage 3 is the most evolved, with almost half the particles residing in clusters.

vertices of the Voronoi diagram; see Table 2 for the percentages at the chosen stages. Stage 1 is the least evolved particle distribution, with the highest percentage of particles in cells, while Stage 3 is the most evolved distribution, with the highest percentage at and around the vertices.

Figure 22 shows the three stages as point clouds, going from left to right in the evolution.

8.2   Graphs of Betti Numbers

We show the graphs of the Betti numbers as functions of the threshold defining the superlevel set in Figure 23. The graphs are significantly different from the ones we see for the single-scale Voronoi

models in Figure 17. The graphs for β_0 show a gradual transition from two to four peaks. The four peaks in Stage 3 reflect the fact that we have a non-trivial number of particles populating each of the four morphological features (clusters, filaments, walls, and the space in between) so that each population contributes its own peak to the graph. As before, the contributions are ordered from left to right as the clusters are densest and merge first, and so on. In contrast to Stage 3, Stage 1 has most particles near the walls and in the space between them, so that there are only two modes in the graph.

A similar trend is also seen in the graphs for β_1. The particle distribution gets progressively more segregated into the morphological features, each with its own density, which explains the clear four peaks we see for Stage 3. The signal we get from β_2 is different while consistent with our explanation. We see one peak at Stage 1 and two peaks each at Stages 2 and 3. As before, the difference is between intra- and inter-structural consolidation, and the second one barely exists in Stage 1, at which time a large fraction of the particles populates the space between the walls.

8.3   Averaged Persistence Diagrams

The evolution of the particle distribution is well visible in the averaged persistence diagrams, which we show separated for the three stages and the different dimensions in Figure 24. Each intensity
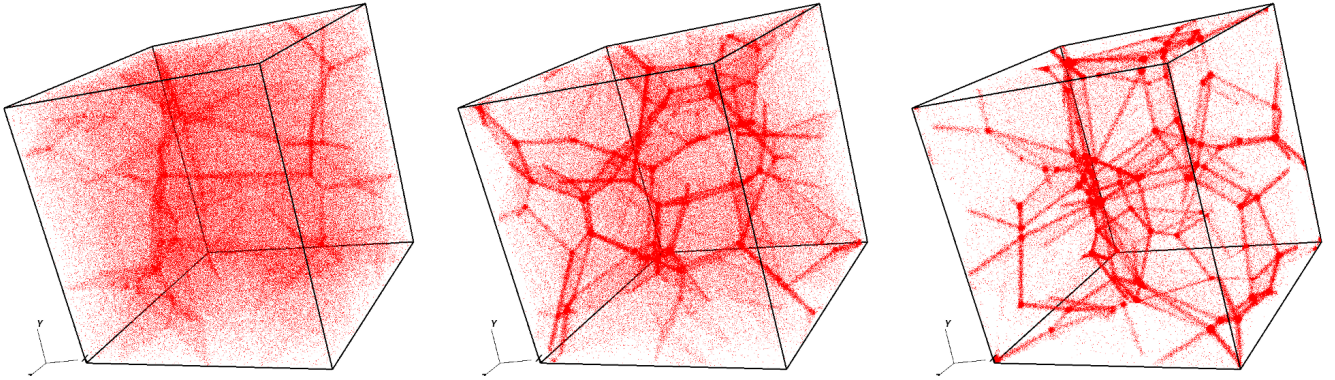
Figure 22. Snap-shots in the Voronoi evolution time-series. Top row, from left to right: particle distribution at the least, medium, most evolved stage. Bottom row, from left to right: volume rendering of the same.
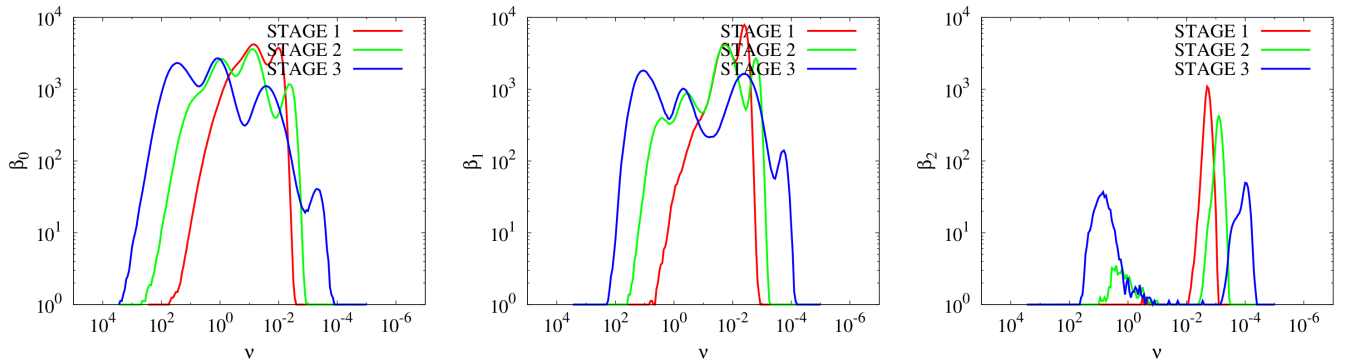

Figure 23. The graphs of the Betti numbers computed for the density function of evolving particle distributions. From left to right: $\beta_0, \beta_1, \beta_2$ at different stages of the evolution. Stages 1, 2, 3 progress from least, to medium, to most evolved.

map is obtained by averaging eight realizations. While the evolution flows from top to bottom, we show the results for the components, loops, and voids from left to right.

Recall that Stage 1 is dominated by particles distribution near the walls and in the space between the walls. Corresponding to the two peaks of the graph for β_0, we see two tongues in the upper-left intensity map, which shows the averaged diagram for the components. Note that the tongue with higher intensity is on the right hand side, where the mean age is larger. Indeed, the density in the space between the walls is smaller while the population there is larger. Two things happen when we go from Stage 1 to Stage 3: the number of tongues increases to four, and the order of the tongues by intensity is reversed. Similar to the graphs of the Betti numbers, we contribute the four tongues at Stage 3 to a clean segregation of the particles into four morphological elements. The change in order is of course due to the trend to put larger populations of particles into lower-dimensional elements. We point out that the two phenomena are related to each other. The percentage of particles in a morphological component dictates its average density, which, in turn, drives the segregation.

Note also the formation of a low-intensity island in the intensity maps, which breaks from the bulk and migrates towards high persistence values as the model evolves. We see this phenomenon in all three dimensions. The underlying reason is that the cells deplete of particles during the evolution, and the created empty space

favors the appearance of inter-structural consolidation — a manifestation of the structure of the underlying Voronoi skeleton itself — which is represented by the islands.

9 SUMMARY AND DISCUSSION

In this study we have described and introduced a multiscale topological description of the Megaparsec cosmic matter distribution. Emanating from algebraic topology and Morse theory, Betti numbers and topological persistence (Edelsbrunner & Harer 2010) offer a powerful means of describing the rich connectivity structure the Cosmic Web. They represent a major extension and deepening of the cosmologically familiar topological genus measure, and the related geometric Minkowski functionals, and are more tuned towards the analysis of the complex spatial weblike and multiscale arrangement of matter and galaxies in the cosmic web.

With the intention to use Betti numbers and topological persistence to analyze the large scale galaxy and matter distribution, this study is a first in a series of publications towards this goal. The present paper has three aims. The first is the presentation of the mathematical foundation. The second aim is the presentation and discussion of the algorithms for computing Betti numbers and persistence diagrams for a given spatial distribution of points, galaxies or simulation particles or objects. The third aspect concerns a systematic exploration of the imprint of different weblike morpholo-
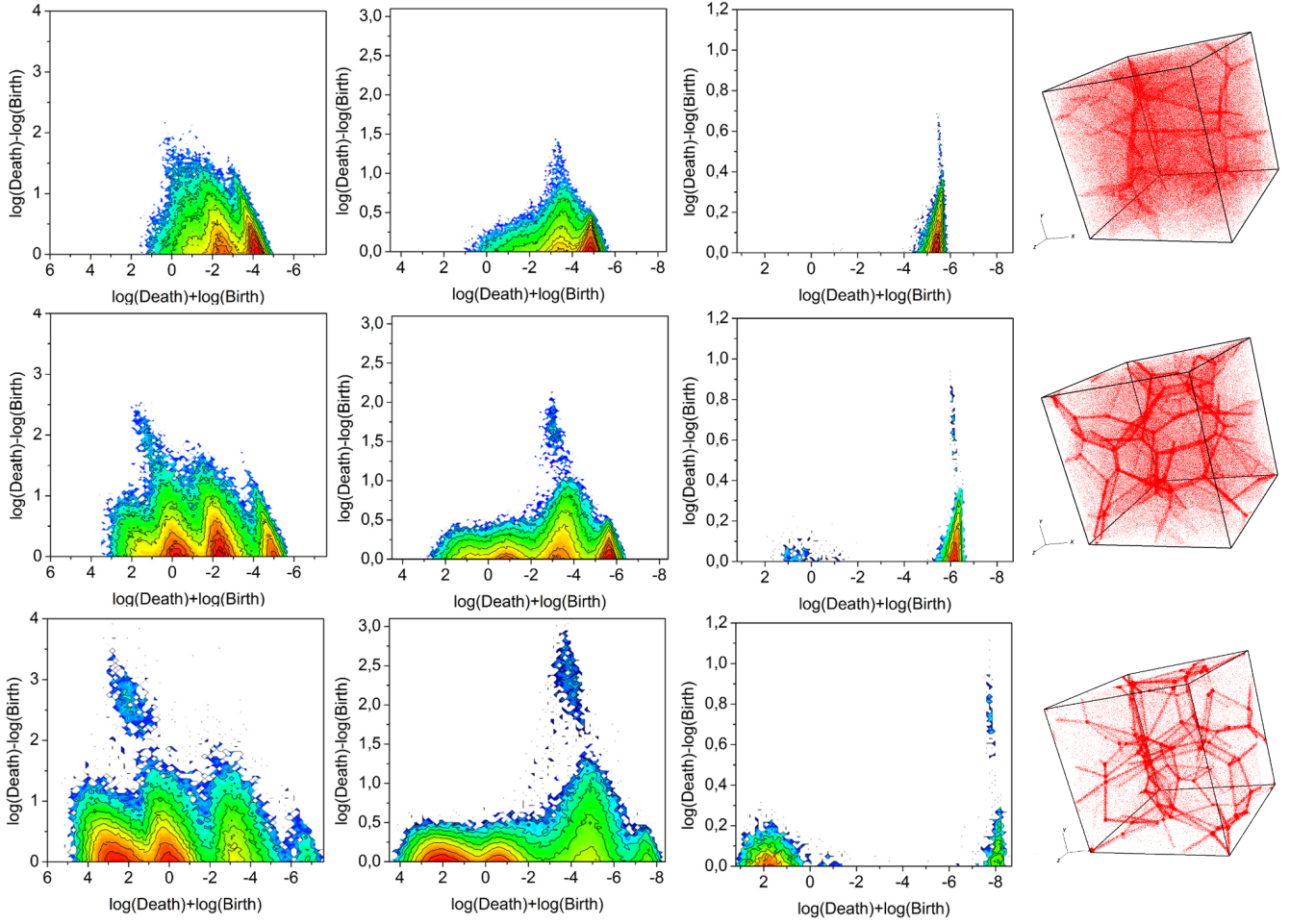
Figure 24. The averaged persistence diagrams of the density function for the Voronoi evolution models. From top to bottom, we show the intensity maps for least, medium, most evolved stages, and from left to right for classes of dimension $0, 1, 2$.

gies and different levels and patterns of multiscale clustering in the computed Betti numbers and persistence diagrams.

The specific formalism from algebraic topology that we use to describe the topological structure of the cosmic mass distribution is known as *homology*. This is the mathematical formalism for the quantitative characterization of the connectivity of space by assessing the presence and identity of holes in a topological space, usually via the descripton of the boundaries of these holes. For a given superlevel set of the cosmic density field, Betti numbers are topological invariants that quantify the presence of isolated islands, tunnels and cavities or enclosed void regions. They have a direct relation to the more conventionally known Euler characteristic, but extend its description of the global topology as it entails, for a 3D density field, 3 independent numbers.

The details of the spatial connections between the various topological spaces, holes or boundaries leads to the concept of *persistence* (Edelsbrunner & Harer 2010). Persistence formalizes topology as a hierarchical concept, and represents a major extension of the available topological machinery to characterize the cosmic mass distribution. Using the singularity structure of a density field, and the realization that the topology of a space is entirely — and only — determined by its critical points, persistence maps the changes in topology that occur at these points. By identifying the formation of new topological features and the destruction of ex-

isting features at each of the critical points, persistence produces a quantitative characterization of the multiscale topological structure of the cosmic web in terms of the *birth* and *death* of topological features. These are summarized in a *persistence diagram*, one for each class of *p*-dimensional topological holes (Edelsbrunner & Harer 2010). In our study we introduce and use *persistence intensity maps*, continuous maps representing an empirical probabilistic description of persistence diagrams.

As for the computational formalism, a major complication enters via the fact of having to deal with a discrete point sample of an underlying density field, while the underlying theory is based on a continuous density field. To this end, we translate the sample point distribution into a piecewise linear continuous density field reconstruction by means of the DTFE algorithm (Schaap & van de Weygaert 2000). On the basis of its representation on the corresponding Delaunay tessellation, the boundary relations between its simplices — tetrahedral cells, triangular faces, edges and vertices — are transformed into a boundary matrix, using the density value estimates at the vertices to evaluate which simplices belong to the density superlevel set at a given density threshold level. Reduction of the boundary matrix translates directly into the set of corresponding pairs of birth-death pairs of topological features, or merger events of separate features, in the persistence diagrams.

An important aspect of the present study is the development

of an understanding of the impact of various key characteristics of the cosmic web on the statistics of Betti numbers and persistence. This forms a necessary step in the application of these to the observed reality of galaxy surveys or fully fledged cosmological N-body simulations. Because analytical expressions for Betti numbers and persistence do not exist for any cosmologically representative situation, not even for Gaussian random fields (but see Feldbrugge et al. (2015)), we use a set of heuristic models of spatial clustering to investigate the influence of a range of morphological features on topological measures.

The first reference template is that of Betti numbers and persistence for uniform distributions sampled from a Poisson point process. The topological imprint of such random featureless distributions also informs us of the contribution by shot noise in generic features sampled by discrete points. Subsequently, we invoke a set of Voronoi clustering models (van de Weygaert & Icke 1989; van de Weygaert 2002) to study the topology measures in a range of weblike galaxy distributions, each differing in prominence of wall-like planes, elongated filaments, cluster nodes or underdense void regions. The influence of the multiscale mass distribution, the result of the hierarchical buildup of cosmic structure, is explored on the basis of the fractal-like Soneira–Peebles model (Soneira & Peebles 1978).

We find that the dominant presence of the various morphological features in the Voronoi clustering models is clearly reflected in the persistence intensity maps. The presence of prominent filamentary structures is particularly strongly manifest in the 1-dimensional persistence diagrams in the form of high persistence cloud. A wall-like distribution, which in Voronoi models goes along with the presence of large voids, induces isolated high persistence clouds in the 2-dimensional persistence diagrams. In the situation wherein most particles are concentrated in and around cluster nodes, we find high persistence clouds in 0-dimensional persistence maps. However, in all situations we find that the discrete nature of the point distributions in the various components of the cosmic web generates a prominent and extended base of low persistence features, that is: features of a low topological significance. In the situation of a multiscale matter distribution, modelled by the fractal Soneira–Peebles model, we find as well a clear manifestation of the clustering properties in the persistence maps and the Betti numbers. Different levels in a nested hierarchy of point clusters reflect themselves in the presence of a sequence of concentrations in a persistence diagram.

In two upcoming studies, we direct the presented topological measures to more realistic cosmological mass distributions. The topology of the dark matter distribution will be addressed in the context of a few large N-body simulations of cosmic structure formation. The relation between the topological characteristics of the dark matter field and the corresponding dark halo distribution is adressed in the same study. It will highlight the expected impact of halo bias on the recorded topological measures, as halos of different masses and assembly epoch trace different parts of the cosmic web. In Nevenzeel (2013) the first results of this study have been presented, pertaining to the topology of the dark matter distribution in cosmologies with a varying nature of dark energy. Also within the context of a large cosmological simulation, a second study combines the dark matter and dark halo topology with that of gas that settled in the cosmic web, and galaxies that emerged in different cosmic environments.

The application of our topological toolbox to the observational reality offers substantial challenges. For the analysis of galaxy surveys we have to deal with measurement errors, selection effects,

systematic biases and errors, substantial shot noise effects, and a range of other practical effects. An important exercise towards this will be assessing the impact of such effects on the topological measurements on the basis of mock galaxy catalogues extracted from standard N-body simulations like the Millennium and Millenium-2 simulations.

Our principal motivation is the understanding of the complex and intricate structure of the cosmic web, the earliest emerging and largest nontrivial structure in the Universe. Nonetheless, persistent topology also opens up a new perspective on the structure of the primordial density field. Homology and persistent topology of Gaussian random fields has been the subject of several insightful studies (Adler & Taylor 2010). In the cosmological context it may provide a rich new characterization of the spatial structure and connectivity in the primordial density field. One issue of high interest is whether the sensitivity of persistence diagrams to slight deviations from Gaussianity, a direct manifestation of inflationary physics, is considerably larger than recorded with more conventional measures. Following a first numerical assessment of Betti numbers in Gaussian fields (Park et al. 2013), it forms the rationale behind our first theoretical paper on the subject (Feldbrugge et al. 2015). Amongst others, the latter has established approximate analytical expressions describing the behaviour of Betti numbers in two dimensional Gaussian random fields, which may be used to allow the detection of non-Gaussian deviations. In two major studies (Pranav et. al. 2016a,b), we present an extensive numerical study of the topological analysis of Gaussian random fields. These studies present and investigate the Betti numbers, Minkowski functionals and persistence diagrams for Gaussian random field realizations, comprising a range of different power spectra, with the purpose of identifying systematic trends.

In summary, while it has lasted some time before powerful concepts from the abstract mathematical branch of algebraic topology have become available for practical applications, major developments in computational topology and geometry over the past years have made them accessible for applications in a wide range of scientific disciplines. In turn, these were enabled by the surge in necessary computational resources. In this study we have demonstrated the potential for a significantly more versatile topological analysis of the cosmic mass distribution. It has paved the path of interesting applications towards a vast range of cosmologically significant issues, and opens up the possibility of answering several questions on the basis of the new perspectives offered by persistent topology.

REFERENCES

Abel T., Hahn O., Kaehler R., 2012, MNRAS, 427, 61

Adler R., Taylor J., 2010, Random Fields and Geometry. Springer Monographs in Mathematics, Springer

Aragón-Calvo M. A., Jones B. J. T., van de Weygaert R., van der Hulst J. M., 2007a, Astrophys. J. Lett., 655, L5

Aragón-Calvo M. A., Jones B. J. T., van de Weygaert R., van der Hulst J. M., 2007b, Astron. Astrophys., 474, 315

Aragon-Calvo M. A., Szalay A. S., 2013, MNRAS, 428, 3409

Aragón-Calvo M. A., van de Weygaert R., Jones B. J. T., 2010, MNRAS, 408, 2163

Bauer U., Kerber M., Reininghaus J., 2013, ArXiv e-prints

Behroozi P. S., Wechsler R. H., Wu H.-Y., Busha M. T., Klypin A. A., Primack J. R., 2013, Astrophysical Journal, 763, 18

Bendich P., Edelsbrunner H., Kerber M., 2010, IEEE Transactions on Visualization and Computer Graphics, 16, 1251

Betti E., 1871, Ann. Mat. Pura Appl., 2, 140

Bond J. R., Kofman L., Pogosyan D., 1996, Nature, 380, 603

Bond N. A., Strauss M. A., Cen R., 2010, MNRAS, 409, 156

Carlsson G., 2009, Bulletin of the American Mathematical Society, 46, 255

Carlsson G., Zomorodian A., 2009, Discrete & Computational Geometry, 42, 71

Carlsson G., Zomorodian A., Collins A., Guibas L. J., 2005, International Journal of Shape Modeling, 11, 149

Cautun M., van de Weygaert R., Jones B. J. T., 2013, Mon. Not. Royal Astro. Soc., 429, 1286

Cautun M., van de Weygaert R., Jones B. J. T., Frenk C. S., 2014, Mon. Not. Royal Astro. Soc., 441, 2923

Cautun M. C., van de Weygaert R., , 2011, The DTFE public software: The Delaunay Tessellation Field Estimator code

Chazal F., Cohen-Steiner D., Guibas L., Mmoli F., Oudot S., 2009, Computer Graphics Forum, 28, 13931403

Chazal F., Sun J., 2014, in Proceedings of the Thirtieth Annual Symposium on Computational Geometry SOCG'14, Gromov-hausdorff approximation of filament structure using reeb-type graph. ACM, New York, NY, USA, pp 491:491–491:500

Cohen-Steiner D., Edelsbrunner H., Harer J., 2007, Discrete Comput. Geom., 37, 103

Colless M., Peterson B. A., Jackson C. e. a., 2003, ArXiv Astrophysics e-prints

Dey T. K., Edelsbrunner H., Guha S., 1999, in Advances in Discrete and Computational Geometry Computational topology. American Mathematical Society, pp 109–143

Edelsbrunner H., 2001, Geometry and Topology for Mesh Generation. Cambridge Monographs on Applied and Computational Mathematics, Cambridge University Press

Edelsbrunner H., Harer J., 2010, Computational Topology: An Introduction. Applied mathematics, American Mathematical Society

Edelsbrunner H., Kirkpatrick D. G., Seidel R., 1983, IEEE Trans. Information Theory, 29, 551

Edelsbrunner H., Letscher J., Zomorodian A., 2002, Discrete & Computational Geometry, 28, 511

Edelsbrunner H., Mücke E. P., 1994, ACM Trans. Graph., 13, 43

Eldering B., 2005, Topology of Galaxy Models. MSc thesis, University of Groningen

Euler L., 1758, Novi Commentarii academiae scientiarum Petropolitanae, 4, 140

Feldbrugge J., Engelen M. V., van de Weygaert R., Vegter G., Pranav P., Wintraecken M., 2015, to be submitted

Forero-Romero J. E., Hoffman Y., Gottlöber S., Klypin A., Yepes G., 2009, MNRAS, 396, 1815

Genovese C., Perone-Pacifico M., Verdinelli I., Wasserman L., 2010, ArXiv e-prints

González R. E., Padilla N. D., 2010, Mon. Not. Royal Astro. Soc., 407, 1449

Gott III J. R., Dickinson M., Melott A. L., 1986, Astrophysical Journal, 306, 341

Guzzo L., The Vipers Team 2013, The Messenger, 151, 41

Gyulassy A., Kotava N., et al., 2012, IEEE Trans. Vis. & Comp. Graphics, 18, 1549

Hahn O., Carollo C. M., Porciani C., Dekel A., 2007, Mon. Not. Royal Astro. Soc., 381, 41

Hamilton A. J. S., Gott III J. R., Weinberg D., 1986, Astrophysical Journal, 309, 1

Huchra J. P., Macri L. M., Masters K. L. e. a., 2012, Apj Supl., 199, 26

Ishiyama T., Rieder S., et al., 2013, Astrophys. J., 767

Kauffmann G., White S. D. M., 1993, Mon. Not. Royal Astro. Soc., 261

Lacey C., Cole S., 1994, Mon. Not. Royal Astro. Soc., 271, 676

Libeskind N. I., Hoffman Y., Knebe A., Steinmetz M., Gottlöber S., Metuki O., Yepes G., 2012, MNRAS, 421, L137

Martinez V. J., Jones B. J. T., 1990, MNRAS, 242, 517

Mecke K. R., Buchert T., Wagner H., 1994a, Astronomy & Astrophysics, 288, 697

Mecke K. R., Buchert T., Wagner H., 1994b, Astronomy & Astrophysics, 288, 697

Milnor J., 1963, Journal of Mathematical Physics

Munkres J., 1984, Elements of Algebraic Topology. Advanced book classics, Perseus Books

Nevenzeel K., 2013, Triangulating the Darkness. MSc thesis, University of Groningen

Neyrinck M. C., 2008, Mon. Not. Royal Astro. Soc., 386, 2101

Neyrinck M. C., 2012, MNRAS, 427, 494

Okabe A., Boots B., Sugihara K., Chiu S. N., 2000, Spatial tessellations: Concepts and applications of Voronoi diagrams, 2nd edn. Probability and Statistics, Wiley, NYC

Park C., Pranav P., Chingangbam P., van de Weygaert R., Jones B., Vegter G., Kim I., Hidding J., Hellwing W. A., 2013, Journal of Korean Astronomical Society, 46, 125

Parkinson H., Cole S., Helly J., 2008, Mon. Not. Royal Astro. Soc., 383, 557

Peebles P., 1980, The Large-scale Structure of the Universe. Princeton series in physics, Princeton University Press

Platen E., van de Weygaert R., Jones B. J. T., 2007, MNRAS, 380, 551

Pranav et. al. 2016a, MNRAS, in prep.

Pranav et. al. 2016b, MNRAS, in prep.

Rote G., Vegter G., 2006, Computational Topology: An Introduction. Springer Berlin Heidelberg, Berlin, Heidelberg, pp 277–312

Sahni V., Sathyprakash B., Shandarin S., 1998, Astrophys. J., 507, L109

Schaap W., 2007, The Delaunay Tessellation Field Estimator. Princeton series in physics, PhD Thesis

Schaap W. E., van de Weygaert R., 2000, Astronomy & Astrophysics, 363, L29

Schaye J., Crain R. A., Bower R. G., et. al. 2015, Mon. Not. Royal Astro. Soc., 446, 521

Schmalzing J., Buchert T., 1997, Astrophys. J. Lett., 482, L1+

Schmalzing J., Buchert T., Melott A., Sahni V., Sathyaprakash B.,

Shandarin S., 1999, Astrophys. J., 526, 568

Shandarin S. F., 2011, JCAP, 5, 15

Sheth R. K., van de Weygaert R., 2004, MNRAS, 350, 517

Shivashankar N., Pranav P., Natarajan V., van de Weygaert R., Bos E. G. P., Rieder S., 2016, IEEE Trans. Vis. Comput. Graph., 22, 1745

Soneira R. M., Peebles P. J. E., 1978, Astrophysical Journal, 83, 845

Sousbie T., 2011, MNRAS, 414, 350

Sousbie T., Pichon C., Kawahara H., 2011, MNRAS, 414, 384

Springel V., 2005, MNRAS, 364, 1105

Stoica R., Gregori P., Mateu J., 2005, Stochastic Processes and their Applications

Stoica R. S., Martínez V. J., Saar E., 2010, Astron. & Astrophysics, 510, A38

Sutter P. M., Lavaux G., Wandelt B. D., Weinberg D. H., Warren M. S., Pisani A., 2014, Mon. Not. Royal Astro. Soc., 442, 3127

Tegmark M., Strauss M. A., Blanton M. R., et. al. 2004, Physica Rev. D., 69, 103501

Tempel E., Stoica R. S., Saar E., 2012, Mon. Not. Royal Astro. Soc., p. 138

van de Weygaert R., 1991, Voids and the geometry of large scale structure. PhD thesis, University of Leiden

van de Weygaert R., 1994, Astron. & Astrophysics, 283, 361

van de Weygaert R., 2002, in Plionis M., Cotsakis S., eds, Modern Theoretical and Observational Cosmology Vol. 276 of Astrophysics and Space Science Library, Froth across the Universe. p. 119

van de Weygaert R., 2007, in ISVD '07: Proc. of Symp. on Voronoi Diagrams in Science and Engineering Voronoi tessellations and the cosmic web: Spatial patterns and clustering across the universe. IEEE Computer Society, Washington, DC, USA, pp 230–239

van de Weygaert R., Bond J. R., 2008, in Plionis M., López-Cruz O., Hughes D., eds, A Pan-Chromatic View of Clusters of Galaxies and the Large-Scale Structure Vol. 740 of Lecture Notes in Physics, Berlin Springer Verlag, Clusters and the Theory of the Cosmic Web. p. 335

van de Weygaert R., Icke V., 1989, Astron. & Astrophysics, 213, 1

van de Weygaert R., Platen E., Vegter G., Eldering B., Kruithof N., 2010, International Symposium on Voronoi Diagrams in Science and Engineering, 0, 224

van de Weygaert R., Schaap W., 2009, in Martínez V. J., Saar E., Martínez-González E., Pons-Bordería M.-J., eds, Data Analysis in Cosmology Vol. 665 of Lecture Notes in Physics, Berlin Springer Verlag, The Cosmic Web: Geometric Analysis. pp 291–413

van de Weygaert R., Vegter G., Edelsbrunner H., Jones B. J. T., Pranav P., Park C., Hellwing W. A., Eldering B., Kruithof N., Bos E. G. P. P., Hidding J., Feldbrugge J., ten Have E., van Engelen M., Caroli M., Teillaud M., 2011, Transactions on Computational Science, 14, 60

Vogelsberger M., Genel S., Springel V., Torrey P., Sijacki D., Xu D., Snyder G. F., Bird S., Nelson D., Hernquist L., 2014, ArXiv e-prints

Zomorodian A., Carlsson G., 2005, Discrete & Computational Geometry, 33, 249

Zomorodian A. J., Ablowitz M. J., Davis S. H., Hinch E. J., Iserles A., Ockendon J., Olver P. J., 2005, Topology for Computing (Cambridge Monographs on Applied and Computational Mathematics). Cambridge University Press, New York, NY, USA